

REPORT DOCUMENTATION PAGE

AFRL-SR-BL-TR-98-

Public reporting burden for this collection of information is estimated to average 1 hour per response, including gathering and maintaining the data needed, and completing and reviewing the collection of information. Send to: collection of information, including suggestions for reducing this burden, to Washington Headquarters Services, Directorate for Information Operations and Reports, 1215 Jefferson Davis Highway, Suite 1204, Arlington, VA 22202-4302, and to the Office of Management and Budget, Paperwork

0715

1. AGENCY USE ONLY (Leave blank)		2. REPORT DATE 20 September 1998	3. REPORT Final: 1 Feb '95 - June '98
4. TITLE AND SUBTITLE Advanced Polarimetric Measurements and Analysis with the CSU-CHILL Radar			5. FUNDING NUMBERS F 49620-95-1-0133
6. AUTHOR(S) V.N. Bringi, V. Chandrasekar, J. Hubbert			
7. PERFORMING ORGANIZATION NAME(S) AND ADDRESS(ES) Department of Electrical Engineering Colorado State University Fort Collins, CO 80523			8. PERFORMING ORGANIZATION REPORT NUMBER
9. SPONSORING/MONITORING AGENCY NAME(S) AND ADDRESS(ES) Maj. Paul Bellaire, Jr. Program Manager, Atmospheric Sciences AFOSR/NM 110 Duncan Ave., Suite B115 Bolling AFB Washington, D.C. 20332-0001			10. SPONSORING/MONITORING AGENCY REPORT NUMBER
11. SUPPLEMENTARY NOTES			
12a. DISTRIBUTION/AVAILABILITY STATEMENT Approved for Public Release; Distribution Unlimited.			12b. DISTRIBUTION CODE Reproduced From Best Available Copy
13. ABSTRACT (Maximum 200 words) Abstract - This AFOSR grant played an important role in the validation of polarimetric signatures in severe storms obtained with advanced CSU-CHILL fully polarimetric radar system. Two field programs during the summers of '95 and '96 were conducted involving instrumented chase vehicles for hydrometeor measurements. An unusual flood event in Fort Collins was also captured by radar and these data were analyzed to show the power of polarimetric-based techniques of measuring rainfall. Equipment purchased with this grant enabled the evaluation of transmitting slant 45°/135° and RHC/LHC polarizations on a pulse-to-pulse basis. A simplified variant of this technique is likely to be adopted for the polarimetric upgrade of the WSR-88D system in the future. Thus, this grant played a key role in the evaluation of future NEXRAD modifications in which the DoD has a heavy investment. We also evaluated random phase and polarization coding of the transmitted waveform via simulations and time series analysis for suppressing second-trip echoes, a known problem for the WSR-88D system. The final results from this grant show conclusive evidence that polarimetric techniques are vital to the remote sensing of storm microphysics. The results of this grant are also applicable to the Theatre Weather Radar (TWR) planned by the DoD to provide tactical weather support.			
14. SUBJECT TERMS Weather radar; polarimetric radar techniques; NEXRAD; CSU-CHILL radar; severe storms			15. NUMBER OF PAGES
			16. PRICE CODE
17. SECURITY CLASSIFICATION OF REPORT UNCLASSIFIED	18. SECURITY CLASSIFICATION OF THIS PAGE UNCLASSIFIED	19. SECURITY CLASSIFICATION OF ABSTRACT UNCLASSIFIED	20. LIMITATION OF ABSTRACT UL

**ADVANCED POLARIMETRIC MEASUREMENTS AND
ANALYSIS WITH THE CSU-CHILL WEATHER RADAR**

FINAL REPORT

V.N. Bringi, V. Chandrasekar, and J.C. Hubbert

Colorado State University
Fort Collins, Colorado 80523

September 23, 1998

Table of Contents

1. AFOSR Support and Resulting Publications	2
2. The CHILL Radar and Research Results	3
2.1 Graves power Matrix	4
2.2 Slant 45°Polarization Mode	5
2.3 Hail Observations	5
2.4 Multiple Scattering: Three-body Effects	7
2.4.1 Ground Model	10
2.4.2 Simulation Results	11
2.5 Phase and Polarization Coding of Radar Signals	13
3. Awards/Prizes	15
4. Technology Transfers	16
5. Educational Impact	16
References	17
Figures	19

1 AFOSR Support and Resulting Publications

Title: Advanced Polarimetric Measurements and Analysis
with the CSU-CHILL Weather Radar Facility

Duration: 1 Feb. 1995 to 31 Jan. 1998

Amount: \$200,230.00

Co-PIs: Drs. V.N. Bringi and V. Chandrasekar

Publications:

1. Hubbert, J., V. N. Bringi, L. Carey and S. Bolen, 1998a: S-band Polarimetric Measurements from a Severe Hailstorm in Eastern Colorado, *J. Appl. Meteor.*, 37, 749-775.
2. Bolen, S., V. N. Bringi and V. Chandrasekar, 1998: An Optimal Area Approach to Inter-comparing Polarimetric Radar Rain Rate Algorithms, *J. Atmos. and Oceanic Technol.*, 15, 605-623.
3. Mudukutore, A., V. Chandrasekar and R. J. Keeler, 1998: Pulse Compression for Weather Radars, *Trans. IEEE Geoscience and Remote Sensing*, 36(1), 125-142.
4. Doviak R.J., V.N. Bringi, A. Ryzhkov, A. Zahrai and D.S. Zrnić, 1998: Considerations for polarimetric upgrades to operational WSR-88D radars, Submitted to *J. Atmos. and Oceanic Technol.*
5. Hubbert, J. and V. N. Bringi, 1998b: The effects of three-body scattering on differential reflectivity signatures, Submitted to *J. Atmos. and Oceanic Technol.*
6. Hubbert, J., V. N. Bringi, V. Chandrasekar, M. Schonhuber, HE Urban and W. L. Randeu, 1997: Storm cell intercepts using a mobile 2D-video distrometer in conjunction with the CSU-CHILL radar, *Preprints 25th Conf. Radar Meteor.*, 8-12 Sept., Austin, TX.
7. Bolen, S., V. N. Bringi and V. Chandrasekar, 1997: An assessment of multiparameter radar rain rate algorithms using an optimal area approach, *Proc. IGARSS*, 3-8 August, Singapore.
8. Bolen, S., V. N. Bringi and V. Chandrasekar, 1997: A new approach to compare polarimetric radar data to surface measurements, *Preprints 25th Conf. Radar Meteor.*, 8-12 Sept., Austin, TX.

9. Hubbert, J. and V. N. Bringi, 1997: The effects of three-body scattering on differential reflectivity, *Preprints 25th Conf. Radar Meteor.*, 8-12 Sept., Austin, TX.
10. Brunkow, D., P. C. Kennedy, S. A. Rutledge, V. N. Bringi and V. Chandrasekar, 1997: CSU-CHILL radar status and comparison of available operating modes, *Preprints 25th Conf. Radar Meteor.*, 8-12 Sept., Austin, TX.
11. Huang, G., V. N. Bringi and J. Beaver, 1997: Application of the polarization power matrix in analysis of convective storms, *Preprints 25th Conf. Radar Meteor.*, 8-12 Sept., Austin TX.
12. Zhao, Li, H. Liu, V. Chandrasekar and C. Frush, 1997: Phase and polarization coding of radar signals, *Preprints 25th Conf. Radar Meteor.*, 8-12 Sept., Austin, TX.
13. Abou-El-Magd, V. Chandrasekar, V. N. Bringi and J. W. Strapp, 1997: Simultaneous radar and in-situ aircraft based observations of convective storms: Intercomparison Study, *Proc. IGARSS*, 3-8 Aug., Singapore.

2 The CSU-CHILL Radar and Research Results

In the Spring of 1995 the CSU-CHILL radar was extensively modified to a two transmitter/two receiver system with a new, high performance dual-polarized antenna. This radar measures the polarimetric covariance matrix in the horizontal/vertical basis at S-band. Because of these unique abilities, there has been and will continue to be much interest in the new polarimetric measurands and their application and validity; for example, see Chapter 8 (Section 8.5.2) of Doviak and Zrnić (1993). Fig. 1 shows a block diagram of system which consists of two largely independent transmitters and receivers driven from a common frequency chain. The conventional transmit mode is an alternate sequence of horizontal (H) and vertical (V) polarized pulses separated by the PRT (typically 1 msec). It is also possible to fire both transmitters simultaneously with nearly equal power generating an approximate slant 45° polarization state. The copolar and cross-polar signals are received as shown in Fig. 1 through the two receivers. Not shown in Fig. 1 is a high-frequency solid state transfer switch located just after the LNAs. This allows the copolar or cross-polar signals to be routed to either receiver for maximum flexibility. Typically, the HH, VV signals are routed to the "copolar" receiver, and VH, HV signals are routed to the "cross-polar" receiver. The average transmitted power in each channel is measured and stored on tape. Each day a solar scan is done to calibrate the two *LDR* measurements. Since the radiation from the sun is randomly polarized (at S-band), it excites both channels with equal power and permits the calculation of

the differential receive gain between channels. Accurately calibrated Z_{dr} data are obtained as the difference between the two LDR^m measurements as follows (in absence of propagation effects):

$$Z_{dr} = dLDR = (LDR_{hv}^m - LDR_{vh}^m) - (CAL_{hv} - CAL_{vh}) \quad (1)$$

where LDR_m are the two measured values, and CAL are the two calibration values based on the solar scan data.

2.1 Graves Power Matrix

While Z_{dr} is strongly dependent on the mean canting angle of spheroids, the asymmetry ratio (A) defined by Kwiatkowski et al. (1995) is not affected but the mean canting angle, and thus it is important to compare A with Z_{dr} in different precipitation types. The asymmetry ratio is the ratio of the maximum and minimum eigenvalues of the 2×2 Graves power matrix ($G = S^* S$, where S scattering matrix). Fig. 2a shows A versus Z_{dr} scatterplot in heavy rain mixed at times with hail (see also, Huang et al. 1997). Each data point is from a range resolution volume. Note the very close agreement between A and Z_{dr} , especially for $Z_{dr} > 2$ dB which implies that the mean canting angle of raindrops must be very close to zero. The points with $Z_{dr} < 2$ dB are identified as rain mixed with hail where A exceeds Z_{dr} by very small amounts (< 0.5 dB). Fig. 2b shows the scatterplot of $A - Z_{dr}$ versus LDR for the same data set. The solid and dashed lines are simulated values from our scattering model of raindrops (Marshall-Palmer dsd with different rain rates) with mean canting angle ($\bar{\theta}$) zero, and standard deviation $\sigma = 5^\circ, 10^\circ$ and 12.5° (Gaussian distribution in θ and uniform in ϕ). Since rain is characterized by LDR typically < -26 dB, the data show that the standard deviation in canting angle is bounded between $5^\circ - 10^\circ$ with $\bar{\theta} = 0^\circ$. Points with $LDR > -26$ dB have increasing values of $(A - Z_{dr})$ which is indicative of rain mixed with hail (also, refer to points in Fig. 2 with $Z_{dr} \leq 2$ dB).

Oriented ice crystals of planar or columnar types are frequently observed in winter storms. Positive Z_{dr} values (at low elevation angles) are frequently associated with planar crystals. If the canting angle is significant then A will exceed Z_{dr} . Fig. 3 shows $(A - Z_{dr})$ versus LDR as a scatterplot from a winter storm in a region (with positive Z_{dr}) consisting predominately of dendrites. Also shown are scattering model results for oblate spheroids (solid ice) with axis ratio varying between 0.1 to 0.5, and mean canting angle varying from 0° to 45° (the standard deviation of Gaussian model is fixed at 10°). Note that the data points fall within the modeled curves quite nicely. The increase in LDR along any one of the modeled curves occurs with increase in $\bar{\theta}$ from 0° to 45° . For any particular data point we can use A to estimate the mean axis ratio assuming

solid ice density. Then the *LDR* value can be used to estimate the mean canting angle using the modeled curves.

2.2 Slant 45°Polarization Mode

The transmission of slant linear 45°polarization is a technique proposed for evaluation on a prototype WSR-88D system by Drs. Zrnić and Doviak of NOAA/NSSL. To avoid use of a high power polarization switch on the transmitter side, this technique involves transmitting slant 45°polarization state and simultaneously receiving the H and V signals from which Z_{dr} , ϕ_{dp} and ρ_{hv} are estimated. The CSU-CHILL radar was configured to do this recently (Brunkow et al. 1997); however, H and V signals were sequentially sampled through one receiver. The four-panel Fig. 4 compares Z_h , Z_{dr} , ϕ_{dp} and ρ_{hv} from the conventional VH-mode versus the so-called star-mode (simultaneous transmit, alternate receive, i.e., slant 45°polarization on transmit) as profiles of radar parameters versus range through an intense rainstorm. While the Z_h , Z_{dr} and ϕ_{dp} agreement is very good, there is a tendency for star-mode ρ_{hv} to be biased low which we believe is due to depolarization in resolution volumes with large intrinsic *LDR*.

Equipment purchased under this AFOSR grant include a 12-bit I-Q modulator and two power meters to assess the feasibility of transmitting polarization states with equal power in H and V polarized components but with prescribed phase difference (nominally 45°/-45°, or RHC/LHC). This capability was tested in June 1998 and data are being analyzed in collaboration with Prof. Anthony Holt of the University of Essex in the U.K.

2.3 Hail Observations

A surface validation campaign occurred in 1995 where instrumented chase vans were deployed in coordination with the CSU-CHILL radar in order to intercept severe storm cells containing hail (Hubbert et al. 1997, 1998a). One chase van was equipped with a roof-mounted hail catcher net which enabled the determination of time-resolved hail rates and size distributions. Numerous storm cell intercepts were made with this van in small, medium and large hail events. Our goal was to correlate polarimetric signatures such as Z_h , Z_{dr} , *LDR*, ρ_{hv} and K_{dp} with the size and intensity of the hail since the Air Force is interested in operational detection of hail greater than $\frac{3}{4}$ inch with radar. Fig.5 shows radar measurements over the van location in the severe hailstorm of 7 June 1995 which produced golfball-sized hail. Observations of hail size made by Drs. Bringi and Hubbert are marked in Fig. 5c. Visual observations of golfball-sized hail started around 1809 MDT (1000s in Fig. 5c) and ended at around 2000s. The occurrence of negative Z_{dr} is frequently observed in

hailstorms with large hail and is noted over the van between 1200 and 2000s where $Z_{dr} \leq -0.5$ dB. Low ρ_{hv} (≤ 0.93) and high LDR (≥ -18 dB) between 1080 - 1750s also correlate well with golfball-sized hail. From 0 to 1000s, the LDR gradually increases from -27 dB to -20 dB in agreement with visual observations of increasing hail size from pea to marble to golfball. After the large hailfall period, and in agreement with visual observations of reducing hailfall at 2000s, the Z_{dr} shows an increasing trend to positive values, LDR decreases to -27 dB and ρ_{hv} increases to 0.97 - 0.98, all characteristic of the transition from rain mixed with hail to rain only. The storm structure at 1812 MDT (1100s in Fig. 5) is shown in Fig. 6a, b as constant altitude PPIs at 3 km altitude (AGL). The horizontal wind vectors are earth relative and obtained from CSU-CHILL/Denver WSR-88D radars. The bottom panel shows positive Z_{dr} nearly coincident with the peak in the horizontal wind convergence field which we use as a proxy for the location of the low level updraft. The van location is marked with an X in Fig. 6b. Fig. 7 a-d shows vertical sections of Z_h , Z_{dr} , LDR and K_{dp} taken along the line marked AB in Fig. 6b. The area of large hail marked as "a" in Fig. 7c is characterized by large LDR (-13 to 16 dB) and low ρ_{hv} (0.88 - 0.92) in association with high Z_h (60 - 70 dBZ) and negative Z_{dr} . The positive Z_{dr} column with peak Z_{dr} of 2.9 dB at 3.5 km altitude is located on the inflow side marked as "d" in Fig. 7b. The positive column consists of supercooled raindrops ascending in the updraft. In Fig. 7c a region of $LDR \geq -22$ dB (marked as "f") is coincident with the top of the positive Z_{dr} column. This enhanced LDR "cap" is caused by partially-frozen drops and asymmetric wet graupel. The vertical structure of K_{dp} in Fig. 7d shows a positive (0.5 to 1°km^{-1}) column marked as "g". It is coincident with $LDR \geq -22$ dB and is located near the interface between the main hailshaft and the positive Z_{dr} column (marked as "updraft fringe" in Fig. 7d). It is hypothesized that the positive K_{dp} column is caused by drops shed from wet hailstones. Shed drops can be an important source for hailstone embryos.

To further study the persistence of these signatures over time, Fig. 8 shows "swaths" of various radar measurands over time from 1720 - 1833 MDT. Fig. 8a shows a swath of $LDR \geq 20$ dB at 0.5 km altitude (solid lines showing the surface hailswath) overlaid with the swath of $Z_{dr} \geq 1$ dB at 3.5 km altitude (dashed lines showing the positive Z_{dr} column swath). These swaths were created by selecting at each grid point the maximum value from all analyzed volumes between 1720 - 1833 MDT. The positive Z_{dr} swath is located across the main inflow region which places the drop embryos in a favorable location for production of large hail. Fig. 8b shows the swath of $LDR > -25$ dB at 4.5 km altitude (dashed lines showing the enhanced LDR "cap" region alluded to earlier) constrained by $30 < Z_h < 50$ dBZ and $Z_{dr} > 0.5$ dB. This swath is entirely contained within the positive Z_{dr} swath and marks an interface region (-5° to -15°C) composed of a mix of supercooled drops, partially freezing drops and asymmetric wet graupel. Fig. 8b also shows

the swath of $K_{dp} > 0.5^\circ \text{ km}^{-1}$ at 2.5 km altitude (solid lines showing shed drops) constrained by $Z_h > 50 \text{ dBZ}$. This swath is located generally between the large hail swath and the positive Z_{dr} swath, i.e., along the low level updraft/downdraft interface. If our inference that the positive K_{dp} at this level is due to mm-sized drops being shed by wet hail is true, then these drops are in a favorable region to be carried aloft, freeze and become embryos for large hail. Fig. 8c shows a swath of $LDR > -25 \text{ dB}$ at 4.5 km altitude (solid lines showing hail at mid-levels within the main precipitation shaft) constrained by $Z_h > 55 \text{ dBZ}$. Enhanced LDR ($> -25 \text{ dB}$) accompanied by large Z_h could indicate wet growth. Modeling studies show that low density graupel and dry hail typically have $LDR < -25 \text{ dB}$, and wet ice hydrometeors typically have more elevated LDR signatures (Aydin and Zhao, 1990). The locations of enhanced LDR at mid-levels corresponding to wet hail, and the LDR "cap" at the top of the positive Z_{dr} column appear to be consistent with the hail trajectories that originate at midlevels southeast of the updraft core, pass through the LDR "cap" rising to heights of around 7 km (around -20°C) where it is likely that dry growth takes place. The trajectory then likely drops downward along the hail cascade (see Fig. 7a) perhaps undergoing wet growth at midlevels (4-5 km) as marked by enhanced LDR . Similar hail trajectories have been described by Conway and Zrnić (1993) who found a preponderance of frozen drop embryos within a sample of large hailstones collected near the surface predicted by the end points of their trajectories that lead to the largest hail in their case, which are similar to those hypothesized here.

2.4 Multiple Scattering: Three-Body Effects

Under most circumstances multiple scattering effects are negligible in radar meteorology. However, multiple scattering effects have been observed in reflectivity signatures on the back side (away from the radar) of high reflectivity cores ($Z_h > 55 \text{ dBZ}$, approx.) that contain hail. Finger like protrusions of elevated reflectivity are seen which have been termed flare echoes or hail spikes. This type of multiple scattering is called three-body scattering (Zrnić 1987) because of the theorized scattering path where transmitted energy is scattered to ground by the illuminated hail stones, the ground then scatters the energy back toward the main beam where hail stones again scatter some of the energy back toward the radar. Zrnić (1987) modeled three-body scattering via a modified radar equation and was able to predict the decay in intensity of the flare echo with respect to increased range. Shown in Fig. 9 is an example of three-body scattering from DLR's (German Aerospace Agency) C-band radar located at Oberpfaffenhofen, Germany (from Hubbert and Bringi, 1998b).

The top panel shows reflectivity with peak values exceeding 65 dBZ. The three-body flare echo is evident on the right side of the panel, i.e., the direct backscatter for ranges greater than about

90 km is very small so that the seen reflectivity contours are probably due exclusively to three-body scatter. The lower panel shows the associated Z_{dr} field. In the area of three-body scattering, the -1 to 1 dB Z_{dr} contour follows roughly a 45° angle. This contour area separates, in general, positive Z_{dr} values (above) from the negative values (below). This pattern in Z_{dr} is seen quite frequently in flare echoes. Note the extreme values of +9 dB and -5 dB which would be difficult to explain microphysically. The expected value of Z_{dr} is 0 dB which is observed in very light rain or in randomly oriented ice particles.

Since three-body scattering is typically associated with lower reflectivities (e.g. the shown flare echo has $Z_h < 35$ dBZ), possible effects of three-body scattering in storm cores is not well known. Another possible artifact of three-body scattering in Z_{dr} is seen in Fig. 9 underneath the storm core at ranges 79 to 88 km where Z_{dr} is quite negative with values less than -3 dB. Researchers have explained these negative values microphysically, i.e., hail of certain size and shape were assumed to be responsible. Model studies show that vertically oriented conical hail less than about 4 cm (Aydin et al., 1984), vertically oriented oblate hail less than about 4 cm and horizontally oriented oblate hail greater than about 4 cm (Aydin and Zhao, 1990) can produce such Z_{dr} signatures. However, it has not been shown that hail stones actually do fall in an such an oriented fashion that would cause Z_{dr} to be negative and since such negative Z_{dr} signatures are frequently seen in hail shafts, it is difficult to explain microphysically. As an alternate explanation, our three-body scattering calculations show that for larger wet hailstones close to ground level, three-body scattering can bias Z_{dr} negative if ground scatter cross-sections are large.

Zrnić (1987) derived a closed form solution to predict the reflectivity and velocity signatures of three-body scattering associated with flare echoes. His model included several approximations and simplifications which are not appropriate for simulating the effects on Z_{dr} . In contrast, we employ a numerical technique that sums the scattering contributions from all particle pairs that contribute to a particular radar resolution volume to simulate total power from three-body scatter. The geometry is shown in Fig. 10. P_i and P_j represent two hail stones in the main beam of the radar while $r_{i,j}$ represent the distance from $P_{i,j}$ to an incremental ground area and $d_{i,j}$ (not shown) represent the distance from $P_{i,j}$ to the radar. The direct scatter comes from the radar resolution volume, B_m , at a distance R_m from the radar with R_m terminating at the back edge of the precipitation medium of depth of D . The depth of the resolution volume is controlled by the radar transmit pulse width, τ , and receiver bandwidth but is given here by $c\tau/2$ where c is the speed of light. Pairs of scatterers in the radar beam will contribute to the observed echo corresponding to B_m if $2R_m - c\tau \leq d_i + d_j + r_i + r_j \leq 2R_m$. For a given range, R_m and particle pair, $P_{i,j}$, the sum $r_i + r_j$ is constant and thus the loci of particles in 3-space that can contribute to three-body

scattering corresponding to range R_m is described by a three dimensional ellipsoid with $P_{i,j}$ as the foci.

To simplify the calculations, the following assumptions/simplifications are made: 1) the radar beam is considered to be parallel to ground, 2) the radar beam is modeled as a cylinder with a constant power across the beamwidth and, 3) scattering from a particular incremental volume along the radar beam is approximated by a single scatterer located at the center of the volume along the beam axis. Scatter from the hail is modeled by the Mie solution for ice spheres, and for water-coated ice spheres.

Under these approximations the above mentioned ellipsoid will have its $P_{i,j}$ axis parallel to the ground (along the line of sight of the radar). The ellipsoid is defined by the distance from the radar to the back edge of the apparent resolution volume, B_m . Another ellipsoid is defined by the distance from the radar to the front edge of B_m which is $R_m - 150$ m for this study. In this way, two concentric, three-dimensional ellipsoids are defined. Where the ground intersects the concentric ellipsoids is represented by the hatched elliptical shell in Fig. 10. The total power due to three-body scattering corresponding to the B_m resolution volume is found by integrating over all pairs of scatterers that lie in the radar beam and integrating over the corresponding ground areas. Mathematically, for the i^{th} and j^{th} particles,

$$V_{3b} = \frac{g \Omega^T S_j G_k S_i E^t}{(4\pi)^2 (R_i R_j r_i r_j)} \quad (2)$$

where $S_{i,j}$ are 2×2 bistatic scattering matrices for the $P_{i,j}$ particles, G_k is a 2×2 bistatic scattering matrix for a ground element and g represents an overall system gain constant including the transmit power. E^t is a 1×2 transmit vector with $[1 \ 0]^T$ and $[0 \ 1]^T$ representing horizontal and vertical transmit polarization states while Ω is the receive polarization vector of the radar. The scattering matrices for the hail are found from Mie theory and are functions of incident and scattered directions. The total power is found by summing over all particle pairs and over all the corresponding ground areas:

$$P_{3b} = \sum_{i,j} \sum_k |V_{3b}|^2 \quad (3)$$

It is important to note that the left summation is a double summation over all particles pairs which physically means that the three-body scatter path is bi-directional. The direct backscatter power from the resolution volume B_m is calculated for a similar density of scatterers as is used for the

three-body scatter calculations:

$$P_{bs} = \sum_i \frac{g^2 |\mathbf{\Omega}^T \mathbf{S}_i \mathbf{E}^t|^2}{(4\pi)^4 d_i^2} \quad (4)$$

Obviously, summing over a realistic ensemble of hailstones contained in the main beam of a radar would be computationally impossible. To simplify the problem the scatter from a vertical cross section of the radar beam is approximated by a single scatterer located at the center of the volume. Since there is a double summation over particle pairs in Eq. (3) and only a single summation over individual particles in (4), a doubling in the number of particles will increase the power ratio P_{3b}/P_{bs} by 3 dB. The concentration of particles, assumed here to be 1 m^{-3} , is accounted for in the model by increasing the ratio P_{3b}/P_{bs} by the amount P_{inc} :

$$P_{inc} = \frac{\text{desired particle number density}}{\text{used particle number density}}. \quad (5)$$

The number density of hail particles as well as the number density of ground grid points was increased until the sum in Eq. (3) converged.

2.4.1 Ground model

The most difficult and uncertain part of the analysis is the modeling of the ground which may be comprised of trees, shrubs, crops, grasses, roads, buildings, water etc. Clearly scattering cross sections from such collections vary dramatically. In addition, even though many backscatter measurements have been made at S- and C-bands, there is a dearth of bistatic measurements. The only significant recent measurements that we are aware of are reported by Ulaby et al. (1988) for 35 GHz. There are sophisticated modeling techniques that have appeared in the literature (Ulaby et al., 1990, Bahar and Zhang, 1996) but they would be difficult to implement into our model and would not necessarily yield more accurate or informative solutions due to the general unknown and complex nature of the ground. Therefore, for this general study the computational complexity is reduced by employing two analytical models for rough surfaces: 1.) an empirical Lommel-Seeliger model, and 2) a statistical model that treats the surface height above a mean planar surface as a random variable. The used Lommel-Seeliger model (Ruck et al., 1970) has the form,

$$\gamma(\theta_i, \theta_s) = k \frac{\cos \theta_i + \cos \theta_s}{\cos \theta_i \cos \theta_s} \quad (6)$$

where k is a function of the surface properties (but treated as a constant here) and θ_i, θ_s are the incident and scattered angles, respectively. Figure 11 shows the bistatic scattering geometry used

for the ground models. A plot of the backscatter cross-section (i.e., $\theta_i = \theta_s, \phi_s = 180^\circ$) Lommel-Seeliger model is shown in Fig. 12. This model gives a reasonable approximation to measured cross sections of terrain surfaces whose dimensions are considerably greater than wavelength for diffuse scattering but can be invalid for specular scatter (Ruck, et al., 1970). We use it as a first-order approximation where the copolar H-polarization (HH) and copolar V-polarization (VV) bistatic cross sections are equal. The advantage of the model is that it is easy to implement, allows for general quantitative results and lets Z_{dr} calculation be unbiased from ground effects (i.e., $VV=HH$ and $VH=HV$ for ground scatter cross sections).

The statistical model is actually an algebraic combination of two models for rough surfaces: 1) a model valid for slightly rough surfaces, and 2) a model valid for very rough surfaces where slightly rough means that the rms surface height is much less than the wavelength while very rough means that the rms surface height is much greater than the wavelength. Typical terrain surfaces will be composed of roughnesses of both scales for frequencies considered here and thus the models are combined with the resulting model yielding scattering cross sections that give good approximation to experimental data (Ulaby and Dobson, 1989). Importantly, the VV exceeds the HH backscatter cross section which is frequently observed experimentally and is necessary here to obtain significant negative Z_{dr} in hailshafts at near ground levels. The statistical model while giving a more accurate representation of terrain than the above Lommel-Seeliger model is still analytical which thus allows for fairly simple simulations. Details of the statistical model can be found in (Ruck et al. 1970).

Shown in Fig. 13a are backscatter cross sections for the slightly rough surface and the very rough surface models. The slightly rough surface model has the VV cross section greater than the HH cross section for angles greater than about 10° . The very rough surface model has the VV and HH backscatter cross section equal and has larger cross sections for angles less than 10° . The composite model shown in Fig. 13b is found by simply adding the Experimental measurements reported in Ulaby and Dobson (1989) indicate that the composite curves shown in Fig. 13b are quite realistic and furthermore, the curves could be easily increased several dB in magnitude especially at small incidence angles.

2.4.2 Simulation Results

Z_{dr} signatures on the backside of a hailshaft

First the model, which the Lommel-Seeliger ground model, is now used to calculate the three-body Z_{dr} signatures on the backside of a hail shaft. The hail shaft depth, D_p , is 3 km and the hail is modeled as 2 cm solid ice spheres. Shown in Fig. 14 is the ratio of three-body HH power

to three-body VV power as a function of range from the back (away from the radar) of the hail shaft (i.e., 0 km corresponds to the back edge of the hail shaft). The three curves correspond to 3, 5 and 7 km radar beam heights above ground. The curves show that the three-body Z_{dr} values are very high close to the hailshaft and then decrease monotonically with increasing range and become negative. As the height increases, the range at which the Z_{dr} first becomes negative increases. This is similar to what is observed in Fig. 9. Thus, the three-body Z_{dr} signature on the back of hailshafts can be attributed to the angular scattering pattern of the hailstones with no preferential scattering from the ground (i.e., $VV > HH$ ground cross sections) required.

Negative Z_{dr} in hail shafts

The model is now used to investigate Z_{dr} signatures in hailshafts at low elevations. A two-layer model is used for the spherical hail: a solid spherical ice core is covered with a 1 mm liquid water shell which is a typical way to model melting hail (Rasmussen and Heymsfield, 1987). The ground is first described using the Lommel-Seeliger model given by Eq.(6). There are two conditions to be met if three-body scattering is to bias the observed Z_{dr} to negative values: 1) the power due to three-body scattering must be close in magnitude to the power due to direct backscatter and, 2) the VV three-body power must be greater than the HH three-body power in order to cause negative observed Z_{dr} (Z_{dr}^{obs}) with,

$$Z_{dr}^{obs} = 10 \log \left[\frac{P_{hh}^{bs} + P_{hh}^{3b}}{P_{vv}^{bs} + P_{vv}^{3b}} \right] \quad (7)$$

where P_{hh}^{bs} and P_{vv}^{bs} are the direct backscattered copolar powers at H and V incident polarizations (equal for spherical scatterers) and, P_{hh}^{3b} and P_{vv}^{3b} are the three-body copolar powers for H and V incident polarizations, respectively. Suppose that $P_{vv}^{bs} = P_{hh}^{bs} = P_{vv}^{3b} = 2P_{hh}^{3b}$, e.g., the direct back scatter medium consists of randomly oriented hail (intrinsic $Z_{dr} = 0$ dB) with the VV three-body power exceeding the HH three-body power by 3 dB. In this case the $Z_{dr}^{obs} = -1.25$ dB. If the three-body Z_{dr} is made 3 dB more negative, i.e., $P_{vv}^{3b} = 4P_{hh}^{3b}$ instead of $P_{vv}^{3b} = 2P_{hh}^{3b}$, then the three-body VV power can also be 3 dB less, i.e. $P_{vv}^{bs} = P_{hh}^{bs} = 2P_{vv}^{3b}$ and these values still yield $Z_{dr}^{obs} = -1.25$ dB. Thus, the three-body VV power can be 3 dB less than the direct backscatter power and still significantly bias the observed Z_{dr} .

Figure 15 shows modeling results using the Lommel-Seeliger ground model for (a) S-band and (b) C-band. There are three sets of curves in each plot corresponding to radar beam heights at 0.01, 0.1 and 0.5 km heights above. Obviously, if the center of the radar beam is at 0.01 km or 0.1 km, the lower part of the beam would be blocked by the earth (assuming a one degree beamwidth). The model assumes no beam blockage and is meant to demonstrate the effects of low elevation angles.

The horizontal axis is the diameter of the hail while the left vertical axis (solid curves) show the ratio of VV three-body power to VV direct backscatter power (in dB), and the right vertical axis (dashed curves) is three-body Z_{dr} (P_{hh}^{3b}/P_{vv}^{3b}) in dB. The dashed curves are not distinguished since they are similar and show that three-body Z_{dr} is typically close to zero ($|Z_{dr}| < 0.7$ dB) for this model. For S-band $P_{vv}^{3b} > P_{vv}^{bs}$ for $D > 4$ cm at 0.01 km height. At 0.5 km height $P_{vv}^{3b} > P_{vv}^{bs}$ only for $d = 5.5$ cm. The model indicates that hail with diameters of about 5 cm to 6 cm would most likely provide sufficient power in order for the three-body scatter to be large enough to effect the primary backscatter signal. Hail less than about 3.5 cm is much less likely to cause enough three-body power to effect the primary backscatter return. At C-band, however, there is a peak at $D = 2.75$ cm where $P_{vv}^{3b} > P_{vv}^{bs}$ at 0.01, 0.1 and 0.5 km heights with $P_{vv}^{3b}/P_{vv}^{bs} = 22.9$ dB for $h = 0.01$ km. Figure 15 also suggests that three-body scattering effects will be more evident at C-band than at S-band since the occurrence of 2.5 to 3 cm hail is much more common than 5 to 6 cm hail. Since three-body Z_{dr} (dotted curves) are not negative enough to significantly bias Z_{dr}^{obs} , we next use the statistical ground model in order to obtain negative Z_{dr}^{obs} .

Figure 16 is similar to Fig. 15 but with the statistical ground model used in place of the Lommel-Seeliger ground model. The solid curves are similar in shape and magnitude to the solid curves of Fig. 15 and similar conclusions can be drawn. However, the dotted curves, showing three-body Z_{dr} , are now quite negative especially in the resonant regions of interest, i.e., $D > 4$ cm for S-band and $2.5 \text{ cm} < D < 3 \text{ cm}$ for C-band. Thus, the more realistic statistical ground model provides for negative three-body Z_{dr} that can cause Z_{dr}^{obs} to be negative. Again, VV are frequently greater than HH ground cross sections for many different terrain types (Ulaby and Dobson, 1989).

2.5 Phase and Polarization Coding of Radar Signals

Pulsed radar systems process signals that are spaced one PRT apart. However, ambiguities can be introduced in this process if radar returns from multiple targets arrive at the same time. Several methods can be used to distinguish the returns from two different pulses by properly tagging the transmit pulse with an identifier code. One such sample identifier is polarization coding. The transmit pulse polarization is changed between alternate pulses. Another way to code is using random phase coding and systematic phase codes to specifically manipulate the unwanted spectra.

Let us assume that the transmit waveform is coded with random phase between 0 to 2π . Then on return, the random phase can be removed from the first trip echo and the second trip echo gets spread as noise. Similarly, the random phase can be removed from the second trip by removing the appropriate phase shift. The power from the stronger first trip echo contributes to the noise,

and essentially masks the weaker second trip echo signal. Consequently, the second trip echo can barely be observed. To solve this problem, a filter is employed to remove the effects of first trip echo. The overlaid echoes from other range intervals would then appear as white noise (Joe et al., 1995). By applying a filter, and after a recohering process, we can obtain the desired signal. In summary, random phase processing techniques can be used to retrieve multiple trip echoes. The entire process is summarized in Figure 17. Similar to phase coding the alternate pulses can be coded in orthogonal polarization states. If we assume a simple condition of co-polarized receiver, then the second trip echoes will be at the orthogonal polarization state and will be suppressed to the level of polarization isolation of the system. Thus a combination of phase and polarization coding can be used to suppress/recover multiple trip echoes. Dual-polarization radar signals are simulated to estimate the degree of separation that can be achieved with overlaid first and second trip echoes by utilizing phase and polarization coding. The simulation assumes a 8 bit phase shifter. Successful application of random phase coding technique for 2nd trip removal requires integration over a large number of samples. First trip radar signal (256 samples) with mean velocity v_1 (-5 m/s), spectral width 2 m/s, and a second trip radar signal with mean velocity v_2 (5 m/s), spectral width 3 m/s, are simulated with different first-to-second trip power ratios. Then random phase and polarization coding methods are used for the first and second trip echo recovery. The mean velocity and standard error in the velocity estimates are shown in Figure 18. If we use polarization coding in conjunction with random phase coding, we can attain additional 25 to 30 dB of suppression depending on the depolarization ratio (LDR) of the targets. This result can be observed in Figure 18. The first trip can be recovered when the second trip exceeds the first trip power by up to 25 dB. One of the effects of the second trip echo in the presence of polarization coding is that it will contaminate LDR measurement. The relationship between measured and true LDR can be expressed as

$$LDR^M = \frac{LDR^T + PR_{21}}{1 + LDR^T PR_{21}} \quad (8)$$

where PR_{21} is the second-to-first first trip power ratio. Figure 19 shows the relation between the measured and true LDR (LDR^T). Phase/Polarization coding method together with proper filtering can also help to reduce this effect. Figure 20 shows the effect of filtering to improve LDR measurement when the true LDR is -20 dB. Random Phase/Polarization coding has been installed on the CSU-CHILL radar. Limited time series data were collected to study the suppression of unwanted trip echoes. Preliminary results show that phase coding techniques can be used successfully in separating 1^{st} and 2^{nd} trip echoes. We are in the process of implementing the combination of phase and polarization coding to experimentally study the effect of suppression/recovery of multiple trip echoes.

3 Awards/Prizes

In Spring 1997, Prof. Bringi received the College of Engineering's highest research award, i.e., the Abell Award for Research and Graduate Support.

4 Technology Transfers

We have collected data with the CSU-CHILL radar in the so-called STAR mode (simultaneous transmit/alternate receive mode), i.e., based on transmitting slant 45° linear polarization state and receiving the H and V polarization components which approximate the HH and VV components obtained from the conventional alternate H/V transmit mode. These data were analyzed and compared with the conventional mode and shown to Drs. Doviak and Zrnić of the National Severe Storms Laboratory (NSSL) of NOAA. They are currently modifying a prototype WSR-88D radar for polarization upgrades and evaluation and have proposed using modes similar to the STAR mode. The positive results with the CSU-CHILL radar in this mode have greatly assisted them in their ongoing work at NSSL.

We have also implemented the simultaneous transmit/simultaneous receive (STSR) mode and have evaluated this scheme with positive results. These data were also shared with Drs. Doviak and Zrnić for application to future polarimetric upgrades of the WSR-88D.

Prof. Chandrasekar worked on random phase and polarization coding using CSU-CHILL radar which has been used by NCAR (contact: Mr. Chuck Frush) for their ongoing evaluation of coding techniques to mitigate range/velocity ambiguity for WSR-88D systems. Also Dr. Zrnić has proposed discrete phase coding sequence to address this same problem and Prof. Chandrasekar will work on testing this concept on the CSU-CHILL radar very shortly. We have assisted Dr. Ed Brandes of NCAR on implementing and evaluating our specific differential phase algorithm for their S-POL radar. His application is to radar hydrology using polarimetric based rain rate algorithms.

Our latest Mueller matrix based scattering code was delivered to Dr. J. Vivekanandan at NCAR and to Dr. Tom Keenan of BMRC in Australia. Our internally developed radar data analysis software package was requested by Prof. Fred Ogden of the University of Connecticut and by Dr. Tom Keenan of BMRC.

5 Educational Impact

Dr. Scott Bolen of the Rome Laboratory, USAF received his Ph.D. degree in 1997 under the direction of Prof. Bringi. Data for his dissertation was collected with the CSU-CHILL radar and with surface instruments deployed during the summers of 1995 and 1996 and was also benefited by the AFOSR grant which funded the participation of Drs. Bringi, Chandrasekar and Hubbert who supervised the REU students.

References

- [1] Aydin, K., A. Seliga and V.N. Bringi. Differential radar scattering properties of model hail and mixed phase hydrometeors. *Radio Sci.*, 19:58-66, 1984.
- [2] Aydin, K and Y. Zhao. A computational study of polarimetric radar observables in hail. *IEEE Trans. Geosci. Remote Sensing*, 28:412-421, 1990.
- [3] Bhar, E. and Y. Zhang. A new unified full wave approach to evaluate the scattercross sections of composite rough surfaces. *IEEE Trans. Geosci. Remote Sens.*, 34:973-980, 1996.
- [4] Brunkow, D.A., P.C. Kennedy, S.A. Rutledge, V.N. Bringi, and V. Chandrasekar. CSU-CHILL radar status and comparisons of available operating modes. In *Preprints, 28th International Conf. on Radar Meteorology*, Austin, TX., 1997. Amer. Meteor. Soc.
- [5] Conway, J.W., and D.S. Zrnić . A study of embryo production and hailgrowth using dual-Doppler and multiparameter radars. *Mon. Wea. Rev.*, 121:2511-2528, 1993.
- [6] Doviak, R.J. and D.S. Zrnić . *Doppler Radar and Weather Observations*. Academic Press, 2nd edition, 1993.
- [7] Huang, G., V.N. Bringi and J. Beaver. Application of the polarization power matrix in analysis of convective storm data using the CSU-CHILL radar. In *Preprints, 28th International Conf. on Radar Meteorology*, pages 49-48, Austin, TX., 1997. Amer. Meteor. Soc.
- [8] Hubbert, J. and V.N. Bringi, L.D. Carey, and S. Bolen. CSU-CHILL polarimetric radar measurements in a severe hail storm in eastern Colorado. *J. App. Meteor.*, 37:749-775, 1998a.
- [9] Hubbert, J.C., V.N. Bringi, and V. Chandrasekar, M. Schönhuber, H.E. Urban, W.L. Randeu. Convective storm cell intercepts using a mobile 2D-video distrometer in conjunction with the CSU-CHILL radar. In *Preprints, 28th International Conf. on Radar Meteorology*, pages 436-437, Austin, TX., 1997. Amer. Meteor. Soc.
- [10] Joe, P., R. Passarelli, A. Siggia , and J. Scott. Second trip unfolding by phase diversity processing. In *Preprints, 27th International Conf. on Radar Meteorology*, pages 770-772, Vail, CO, 1995. Amer. Meteor. Soc.
- [11] Kwiatkowski J.M., A.B. Kostinski and A.R. Jameson. The use of optimal polarizations for studying the microphysics of precipitation: Nonattenuating wavelengths. *J. of Atmos. and Oceanic Tech.*, 12(1):96-114, Feb. 1995.

- [12] Rasmussen, R.M. and A.J. Heymsfield. Melting and shedding of graupel and hail. Part II: Sensitivity study. *J. Atmos. Sci.*, 44:2764-2782, 1987b.
- [13] Ruck, G., D. Barrick, W. Stuart and C. Krichbaum. *Radar Cross Section Handbook*, volume 2. Plenum Press, New York, 1970.
- [14] Ulaby, F.T. and M.C. Dobson. *Handbook of radar scattering statistics for terrain*. Artech House, Norwood, MA, 1989.
- [15] Ulaby, F.T., T.E. Van Deventer, J.R. East, T.F. Haddock, and M.E. Coluzzi. Millimeter-wave bistatic scattering from the ground and vegetation targets. *IEEE Trans. Geosci. Remote Sensing*, 26:229-243, 1988.
- [16] Zrnić, D.S. . Three-body scattering produces precipitation signature of special diagnostic value. *Radio Sci.*, 22:76-86, 1987.

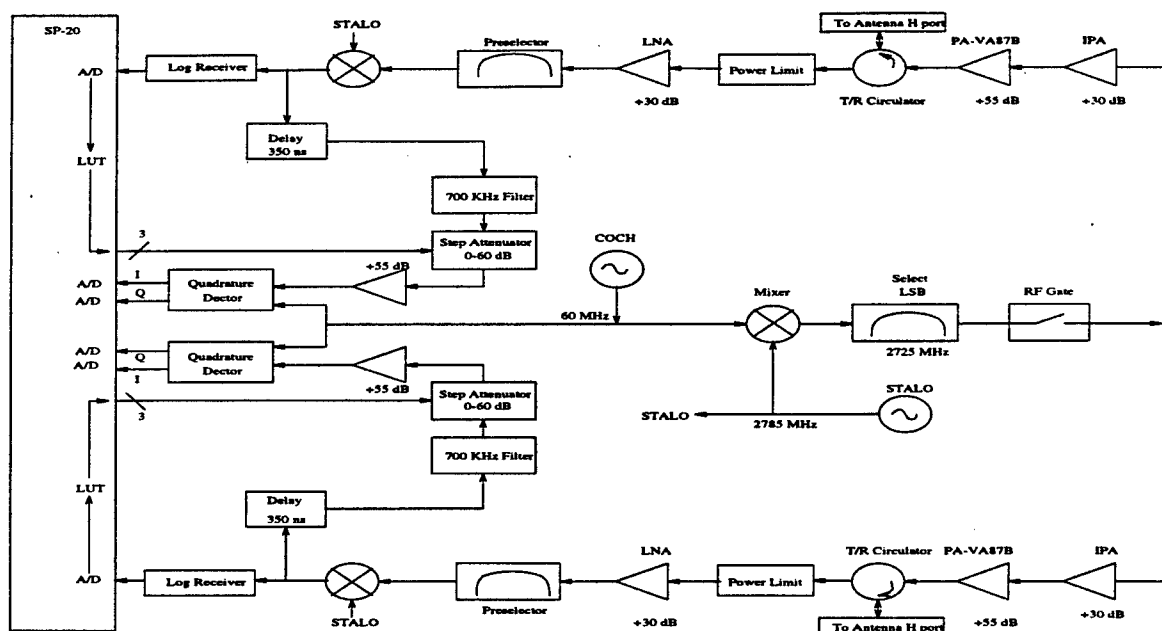


Figure 1: The Block Diagram of the CSU-CHILL Radar.

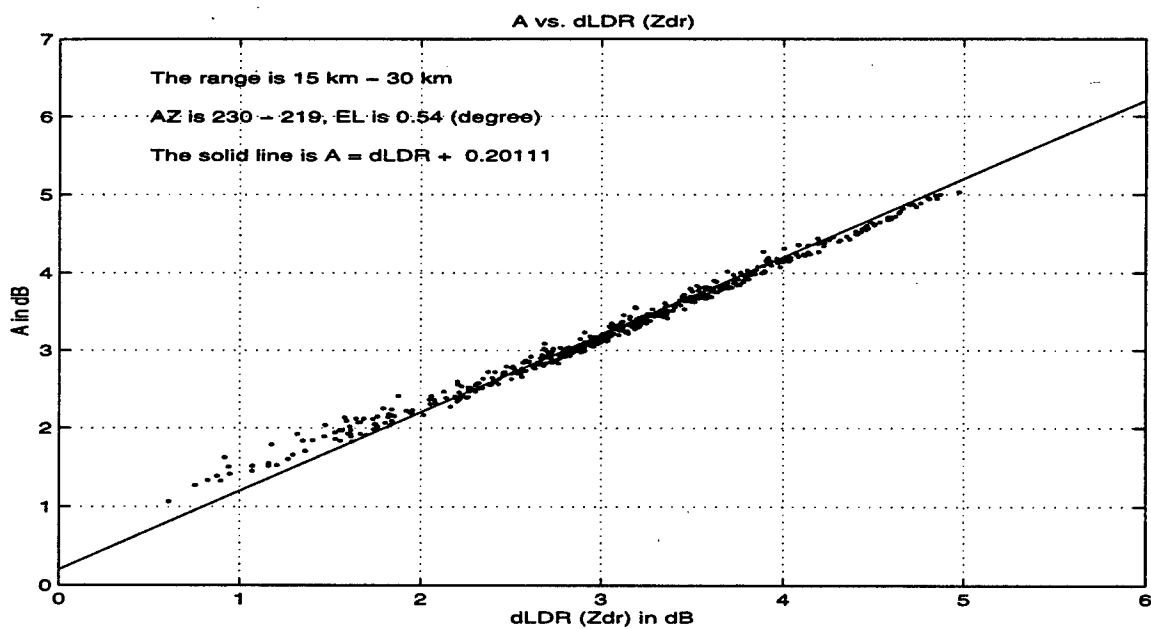


Figure 2: (a) The A vs Z_{dr} Scatter Plot for Rain.

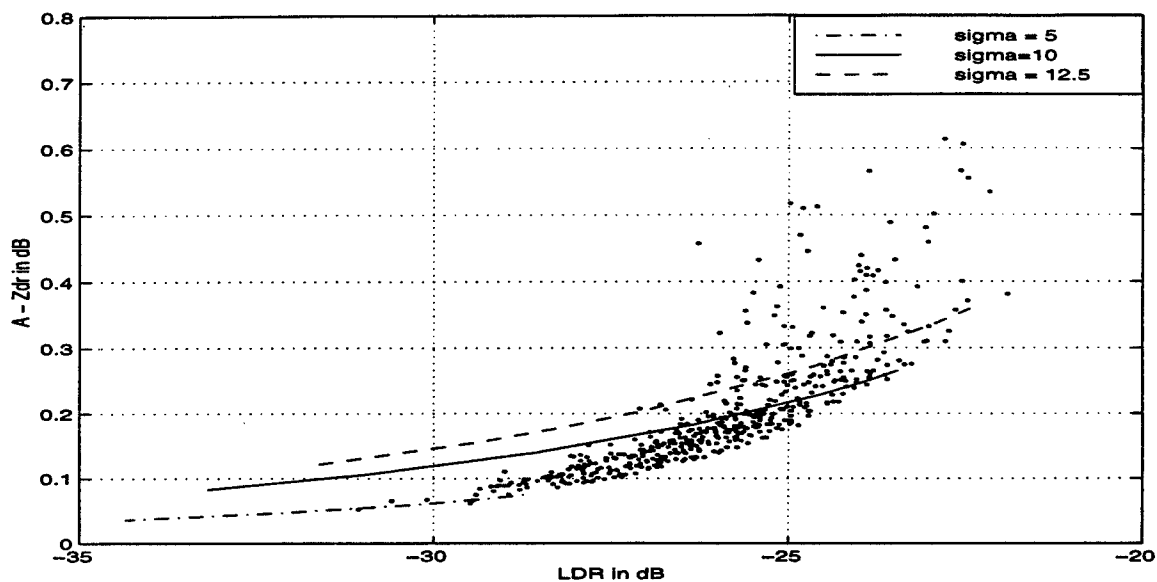


Figure 2: (b) The $A - Z_{dr}$ vs LDR Scatter Plot for Rain.

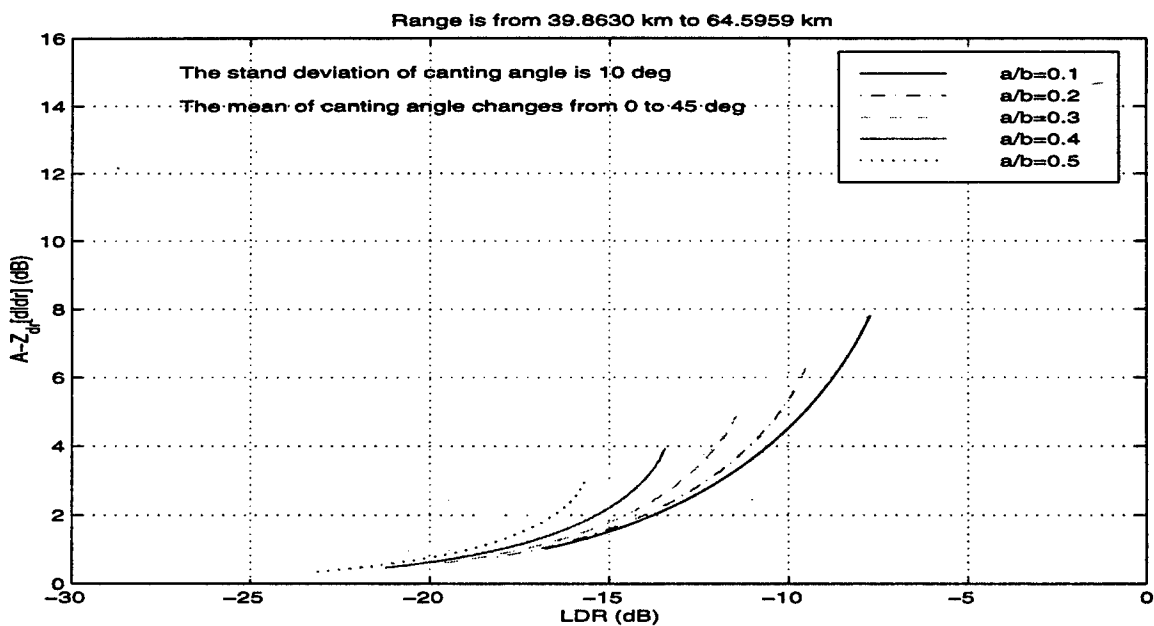


Figure 3: The $A - Z_{dr}$ vs LDR Scatter Plot for winter event.

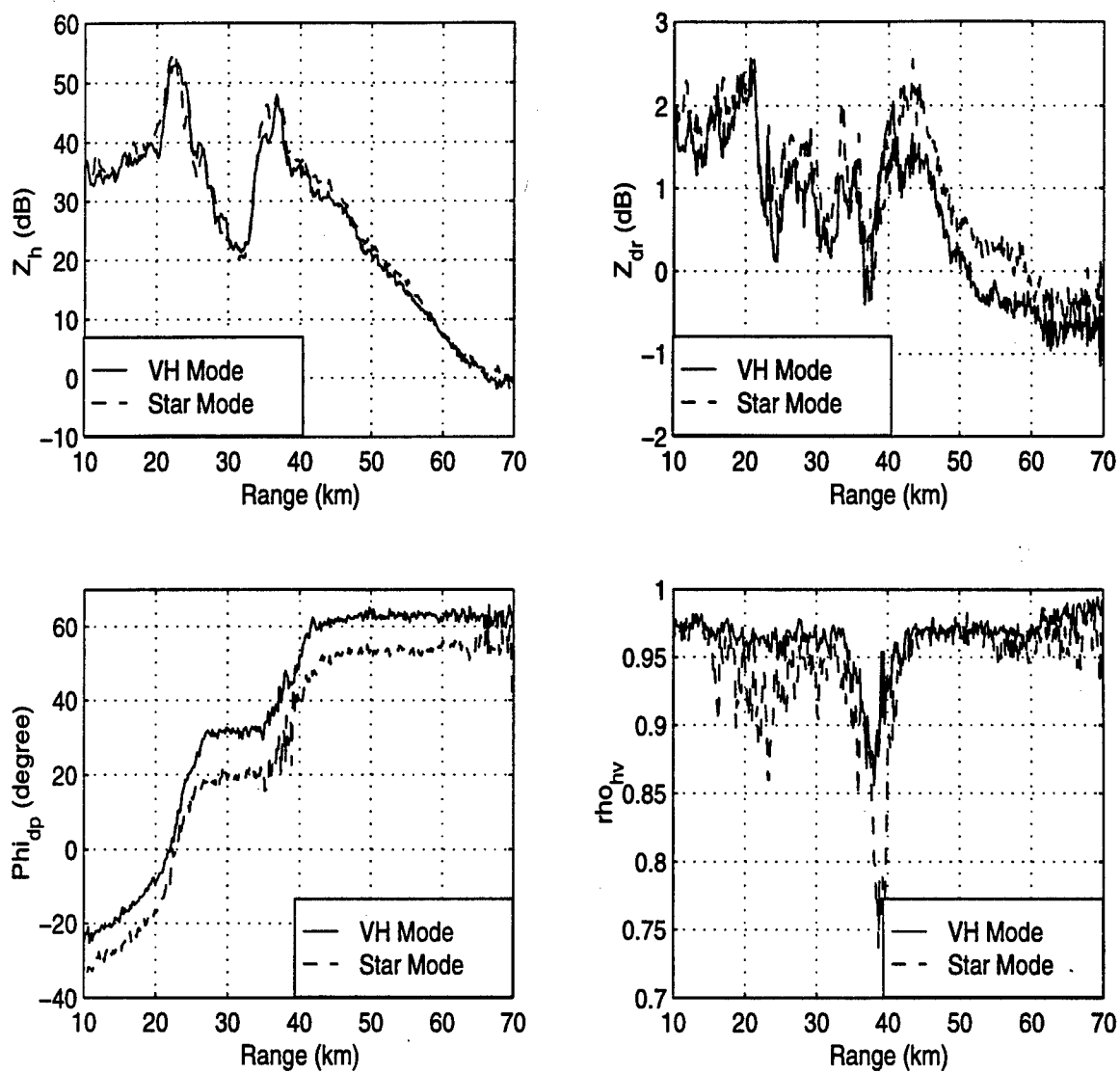


Figure 4: Four-panels comparing VH with Star-mode.

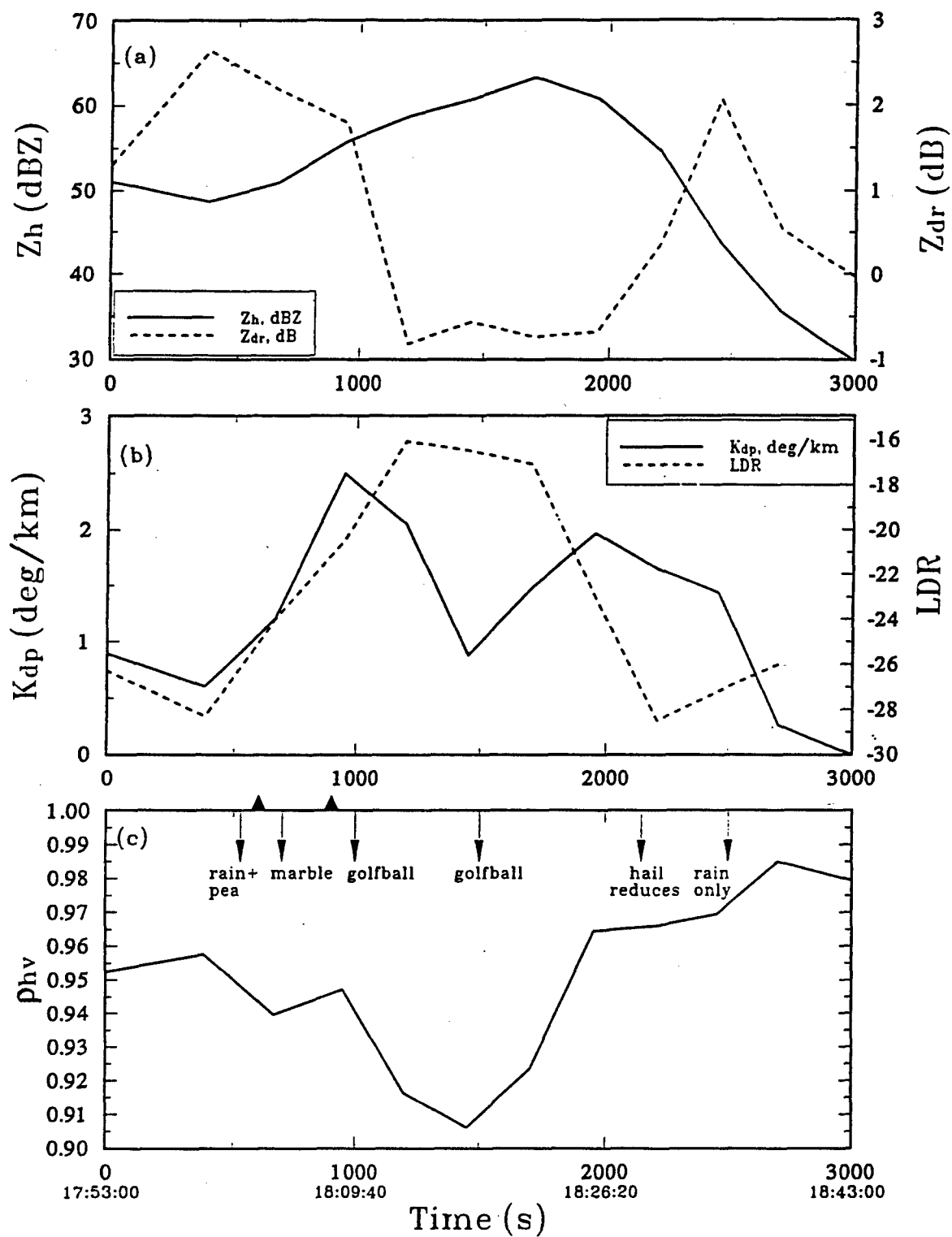


Figure 5: Time series of (a) Z_h and Z_{dr} , (b) K_{dp} and LDR , and (c) ρ_{hv} over the chase van location marked by X in Fig. 6b. Data obtained from the 1° elevation sweep (altitude ≈ 350 m AGL). Except for LDR , the radar values are averaged over a circular area of diameter = 1 km centered over the chase van location. The LDR values are taken from a resolution volume in the 1° elevation angle sweep which is closest to the van location. In panel (c), visual observations (made by van personnel) of hydrometeor type are marked versus time. The two solid triangles mark the time interval 1803-1808 during which hailstones were collected with the hail "catcher" net system.

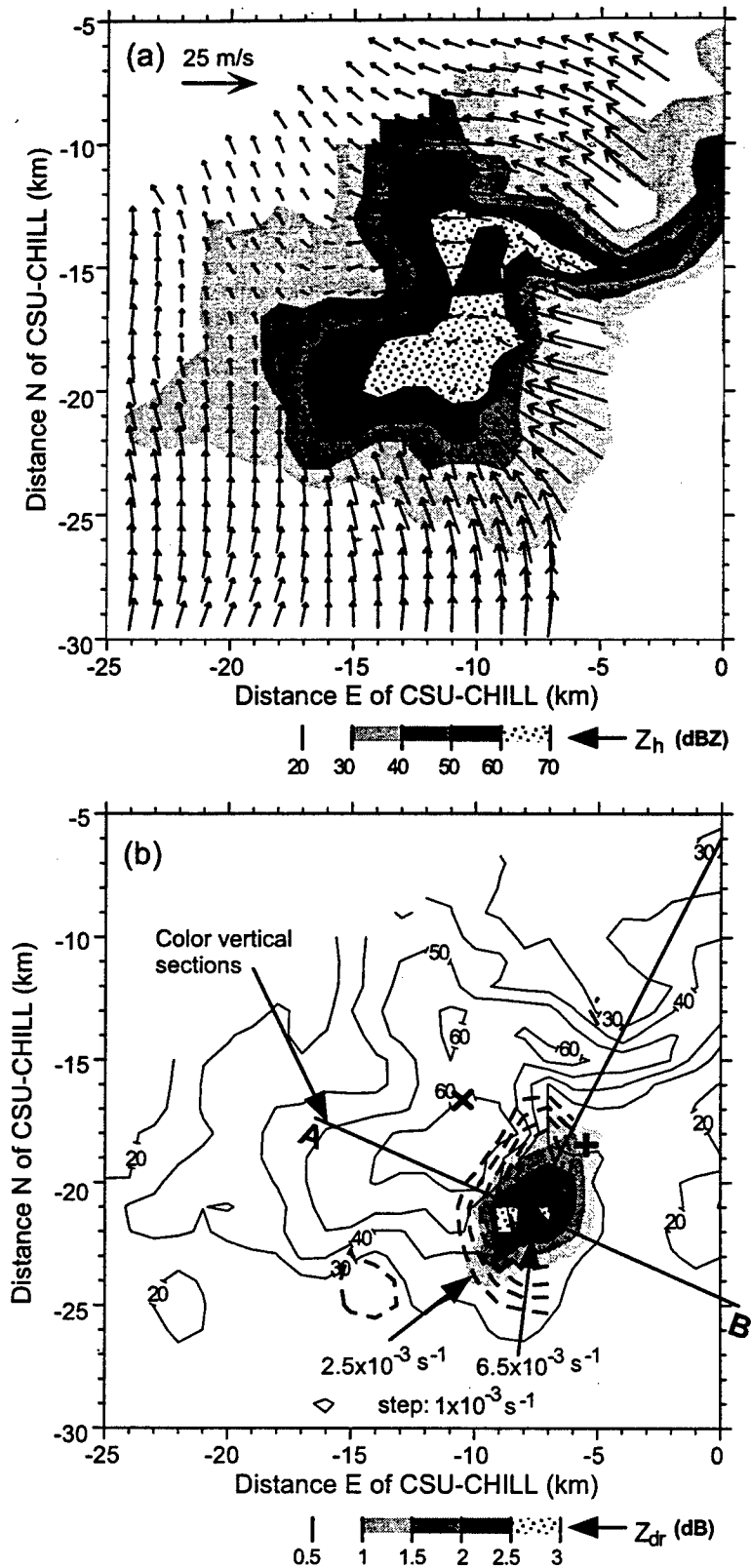


Figure 6: (a) Dual-Doppler synthesized horizontal winds at 1812 MDT from Denver WSR-88D and CSU-CHILL radars at 3km altitude (AGL). Grid origin is at the CSU-CHILL location. Grey-scale filled contours of Z_h from CSU-CHILL start at 20 dBZ and increment by 10 dB. Grid origin is at the CSU-CHILL location. Wind vectors are earth relative. (b) Solid contours represent Z_h . Dashed contours show values of the horizontal convergence field. Grey-scale filled contours of Z_{dr} start at 0.5 dB with step = 0.5 dB. The X marks the chase van location. The solid line marked "A, B" marks the location of the vertical section of Fig. 7.

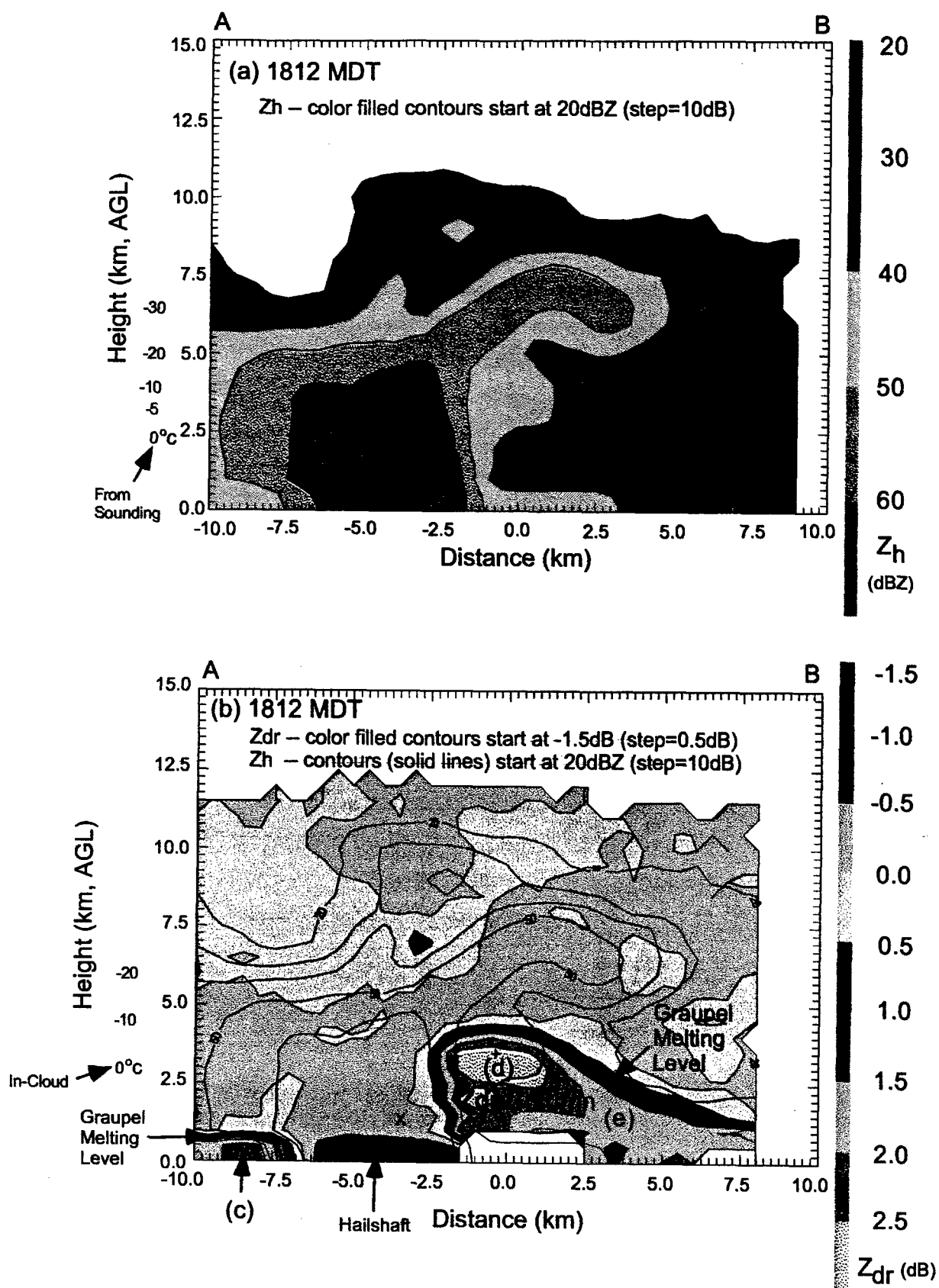


Figure 7: Vertical section of multiparameter radar data at 1812 MDT along the line marked A-B in Fig. 6b. The new grid origin is at (-7.7, -21.1 km) relative to the CSU-CHILL location. (continued on next page)

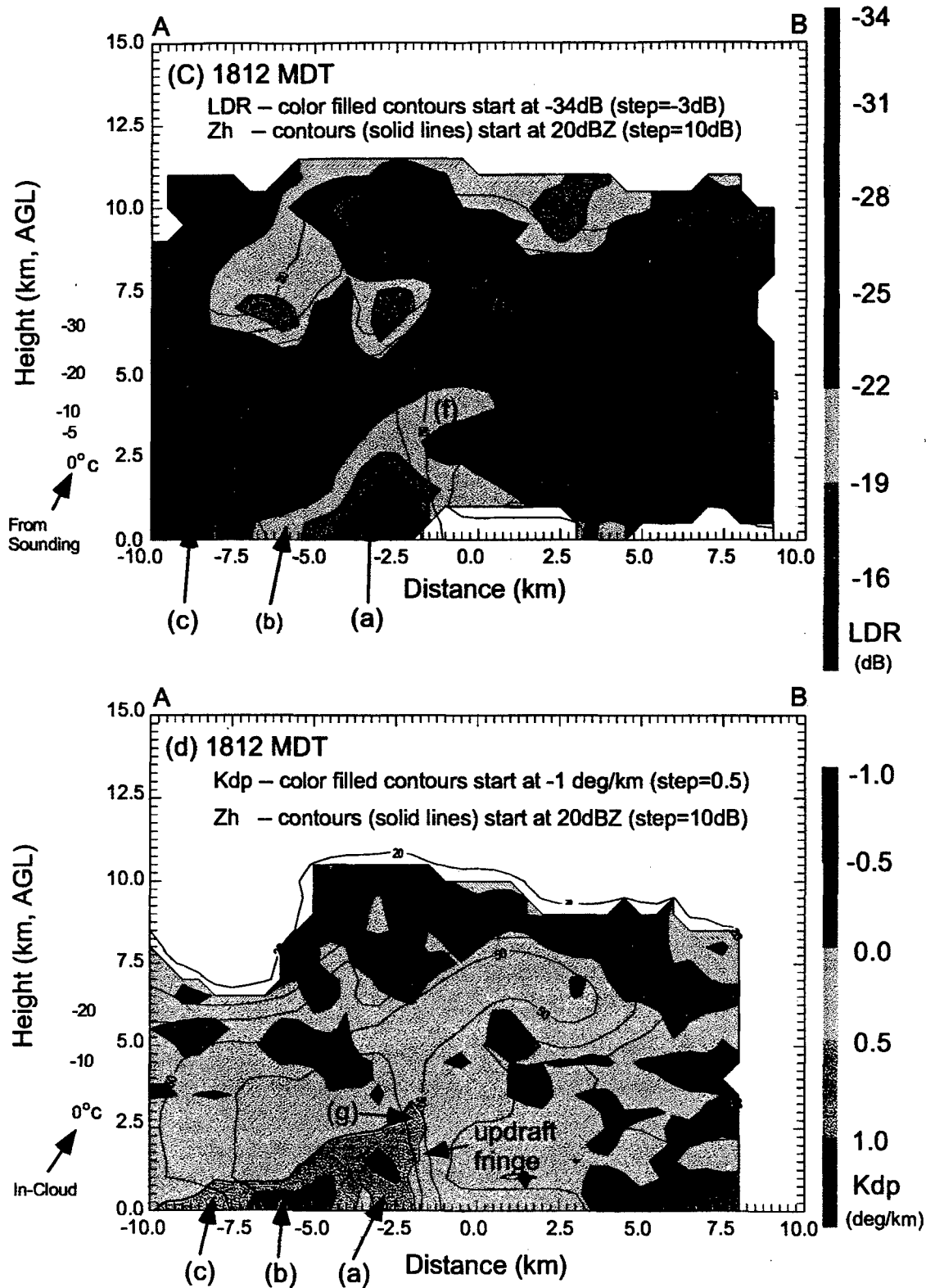


Figure 7: (continued) In Panels a and c the environmental temperature is given as obtained from sounding points. In panel b and d, the in-cloud temperature scale is given. The reflectivity contours from panel a are overlaid on the other fields.

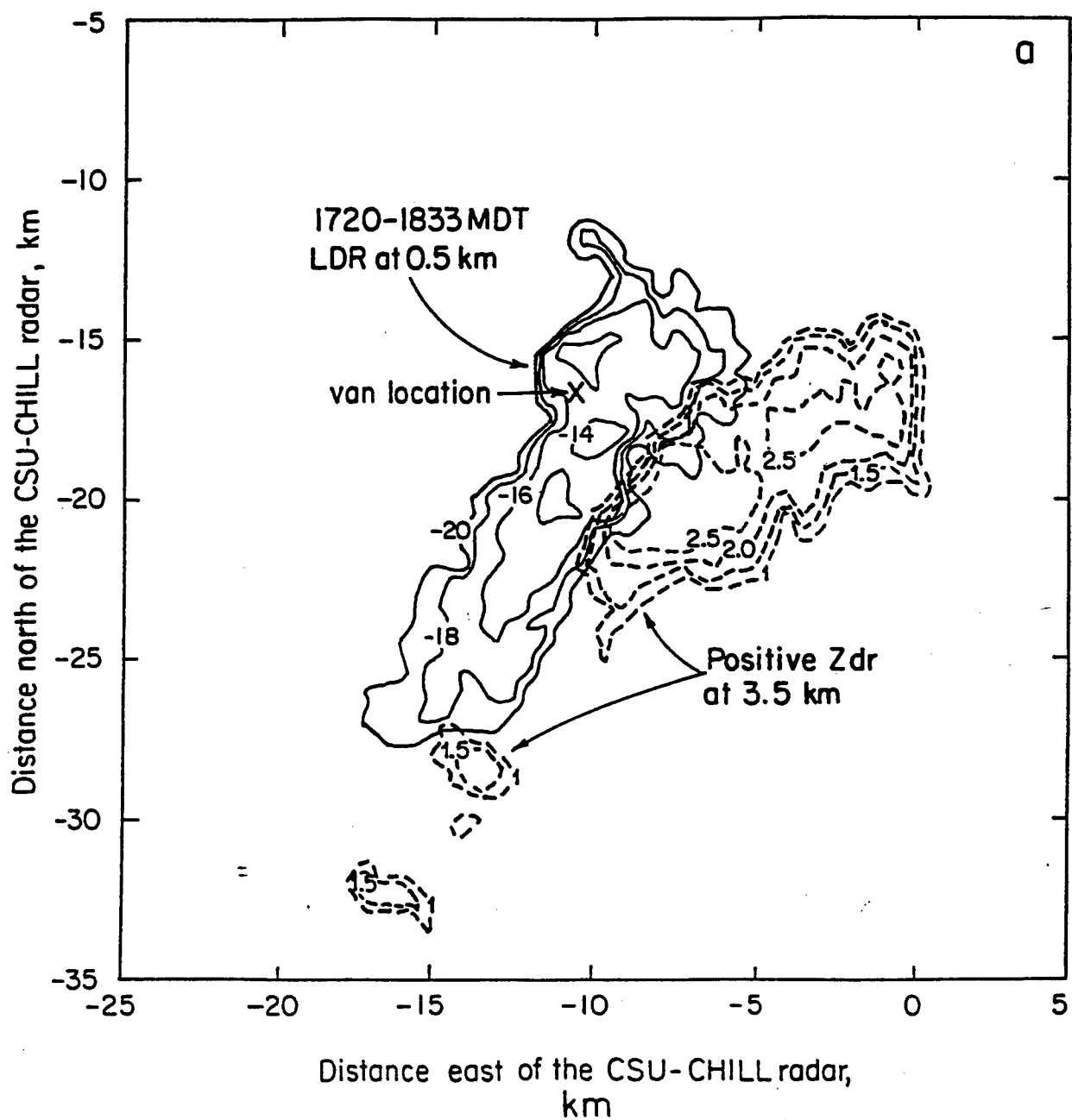


Figure 8: Swaths of radar signatures from 1720 to 1835 MDT. a: $LDR > -20$ dB (solid lines) at 0.5 km level constrained by $Z_h > 55$ dBZ, $Z_{dr} < 0.5$ dB and $\rho_{hv} < 0.95$. It represents the surface hail swath. Dashed lines are swaths of $Z_{dr} > 1.0$ dB at 3.5 km AGL representing the positive Z_{dr} column location with marks, in part, the low level updraft. (continued)

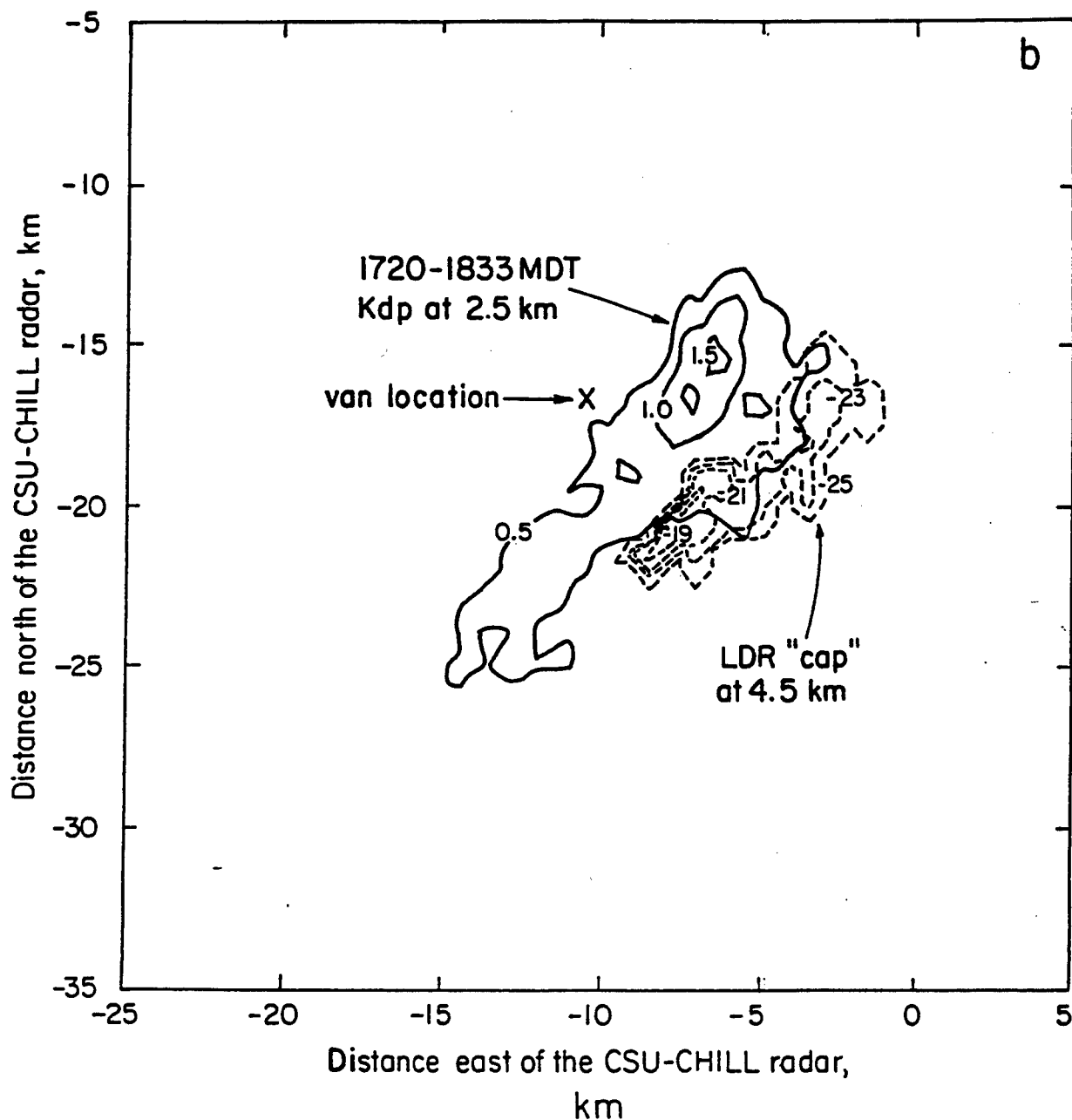


Figure 8: (continued) b: swath of $K_{dp} > 0.5^\circ \text{ km}^{-1}$ at 2.5 km AGL (solid lines) constrained by $Z_h > 55 \text{ dBZ}$. It represents the swath of drops shed by wet hail. Dashed lines show swath of LDR "cap" where $LDR > -25 \text{ dB}$ at 4.5 km AGL constrained by $30 < Z_h < 50 \text{ dBZ}$ and $Z_{dr} > 0.5 \text{ dB}$. It maps the mixed phase interface region.

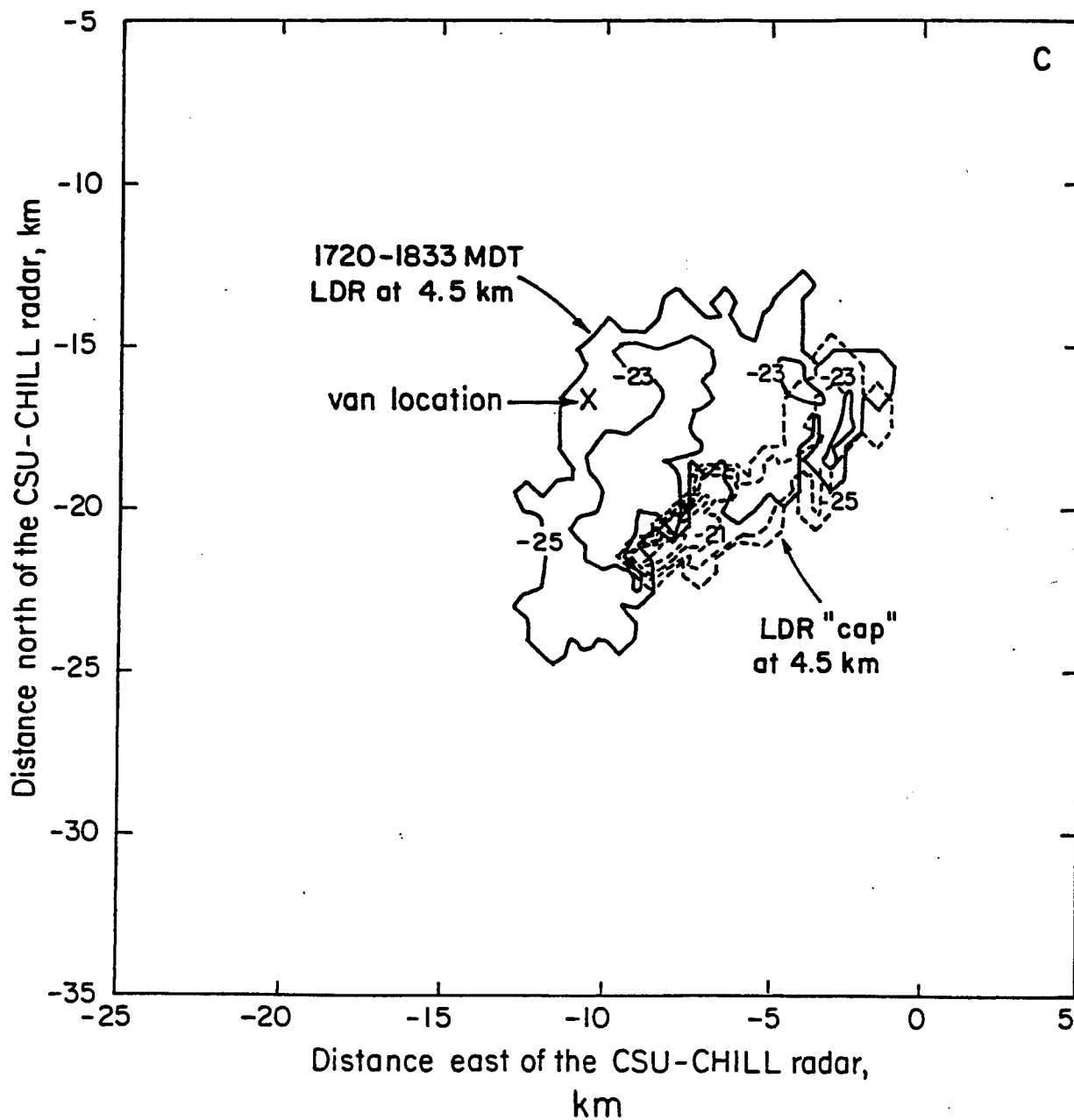


Figure 8: (continued) c: Swath of $LDR > -25$ dB at 4.5 km AGL constrained by $Z_h > 55$ dBZ. It represents the hailswath at mid-levels where the hail is likely experiencing wet/spongy growth. Dashed lines are same as in (b).

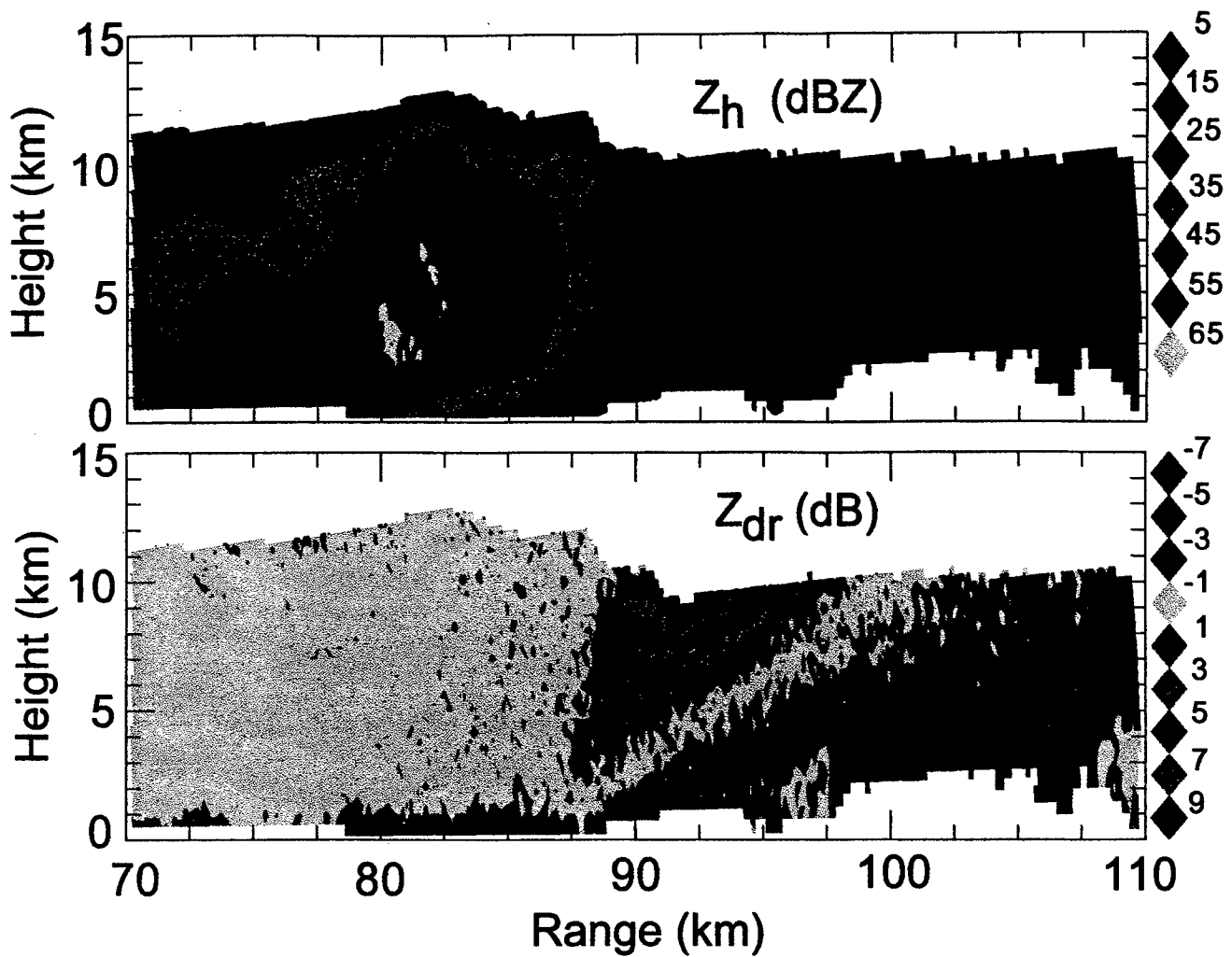


Figure 9: An example of three-body scattering in a hail storm from DLR's (German Aerospace Agency) C-band radar located at Oberpfaffenhofen, Germany. The three-body signature is easily seen as the protruding reflectivity area on the right hand side in the top panel. The bottom panel shows the associated Z_{dr} (differential reflectivity) three-body scatter signature.

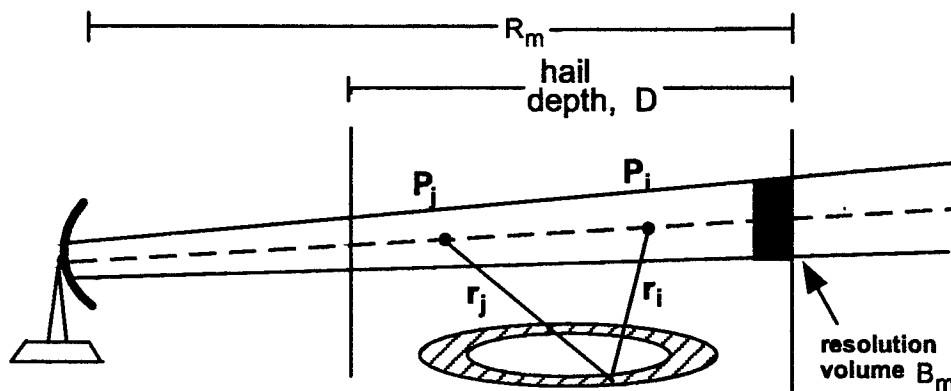


Figure 10: A schematic of three-body scattering. Signal path: radar → particle P_i → ground → particle P_j → radar. The hatched area on the ground represents the area that has the same time delay as resolution volume B_m .

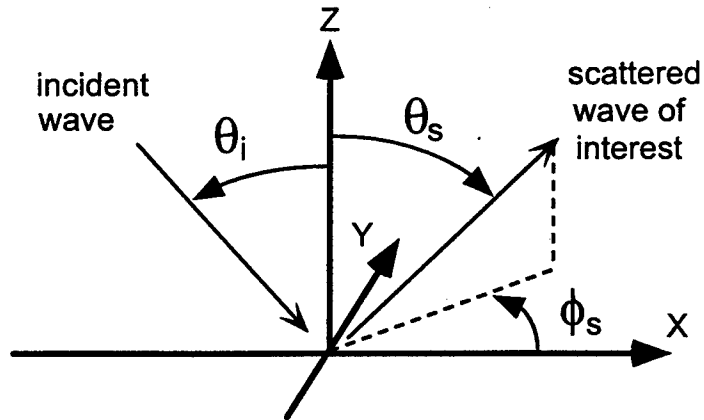


Figure 11: The three-body scattering geometry for a ground element. Incident wave direction is always in the xz plane.

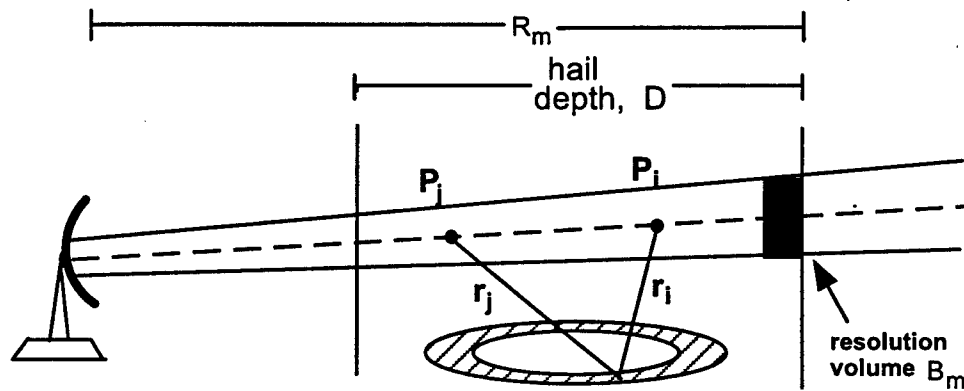


Figure 12: The backscatter cross section $10 \log \gamma$ for the Lommel-Seeliger model (Eq. (6)) for the ground. Note that $\theta_i = \theta_s$ in Fig. 10.

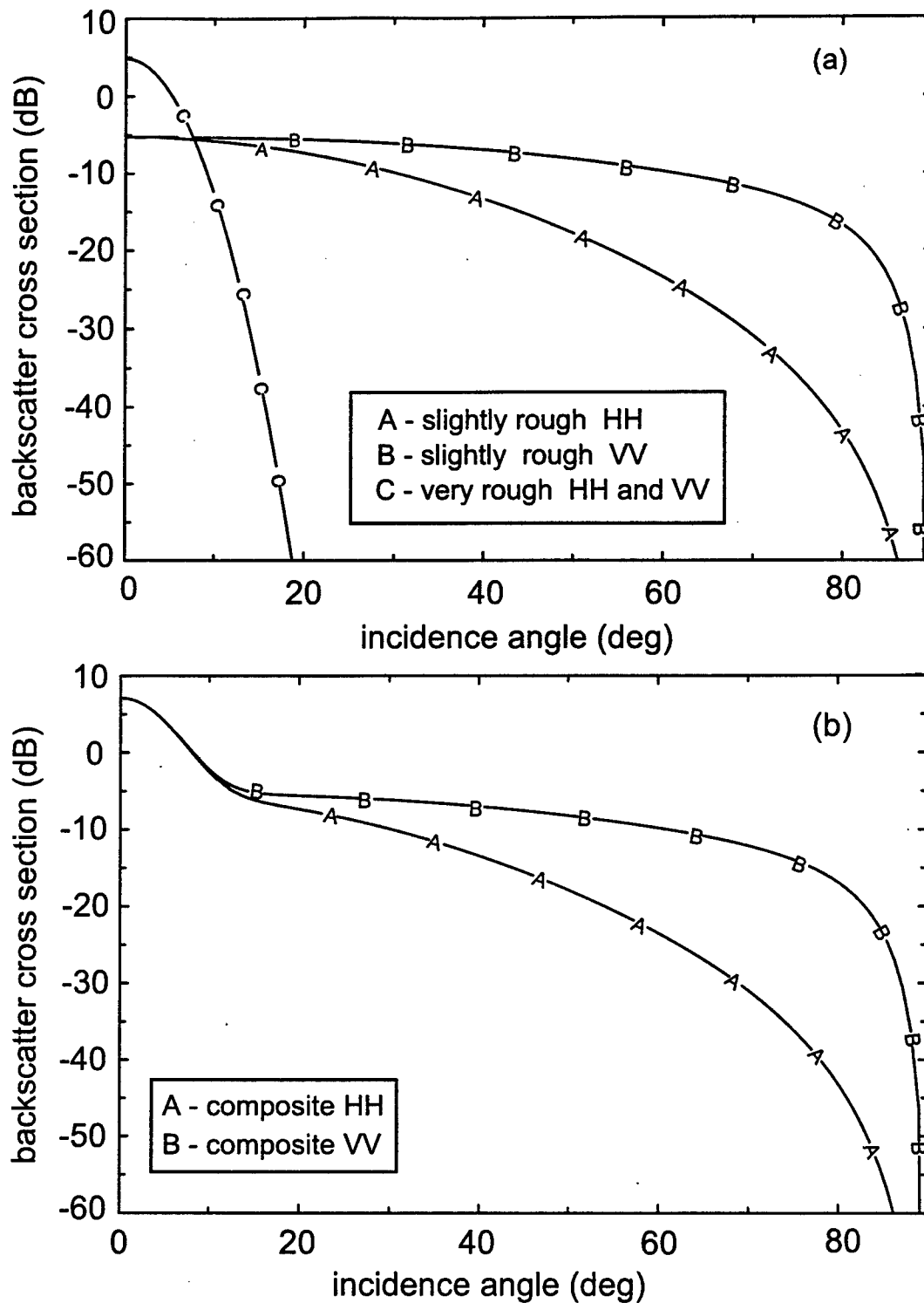


Figure 13: The backscatter cross section ($\theta_i = \theta_s$) for (a) the very rough and slightly rough surface models and (b) the composite model.

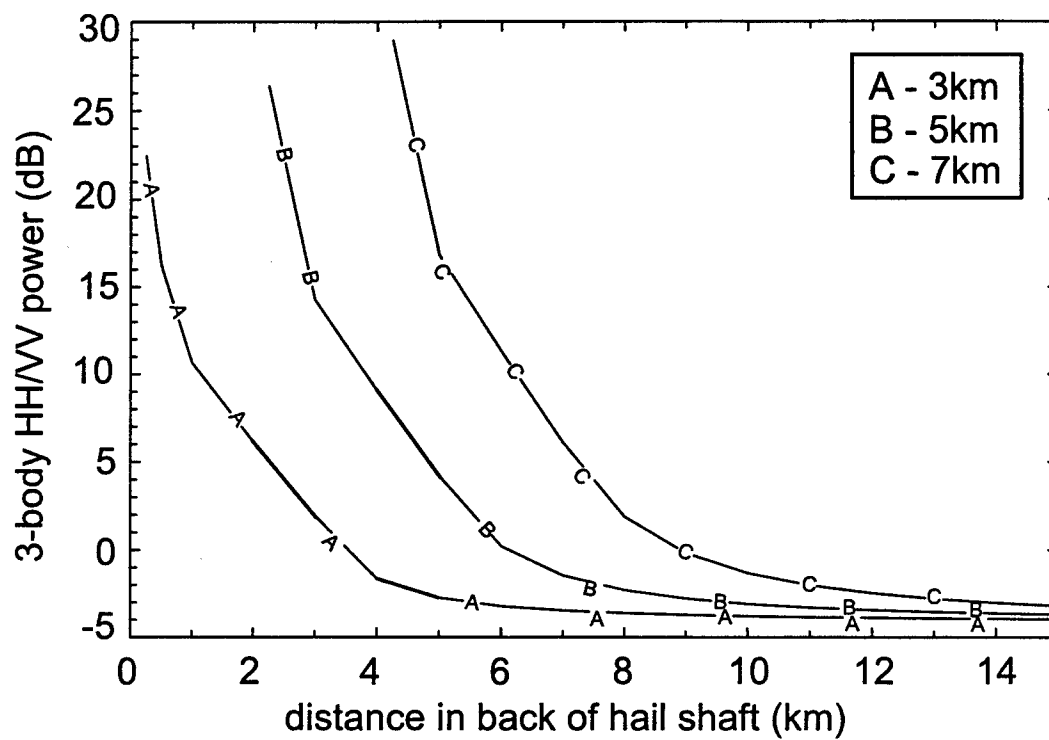


Figure 14: The three-body power ratio HH/VV as a function of distance in back of the hail shaft.

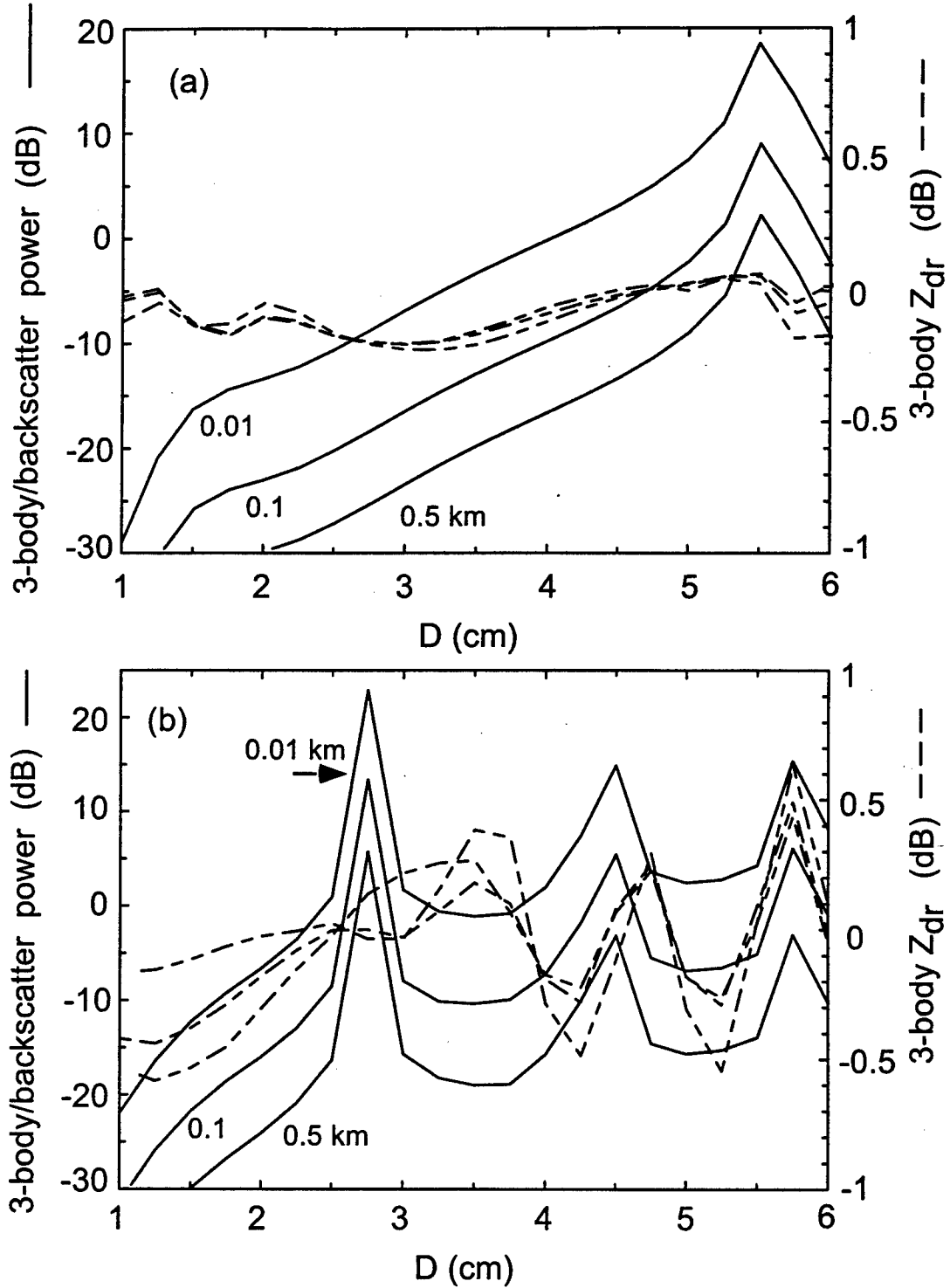


Figure 15: The ratio of three-body scatter power to direct backscatter power (left axis) and three-body Z_{dr} as a function of hail diameter. Spherical hail is modeled as an ice core with a liquid water coat (1 mm). The Lommel-Seeliger ground model is used, (a) S-band (b) C-band.

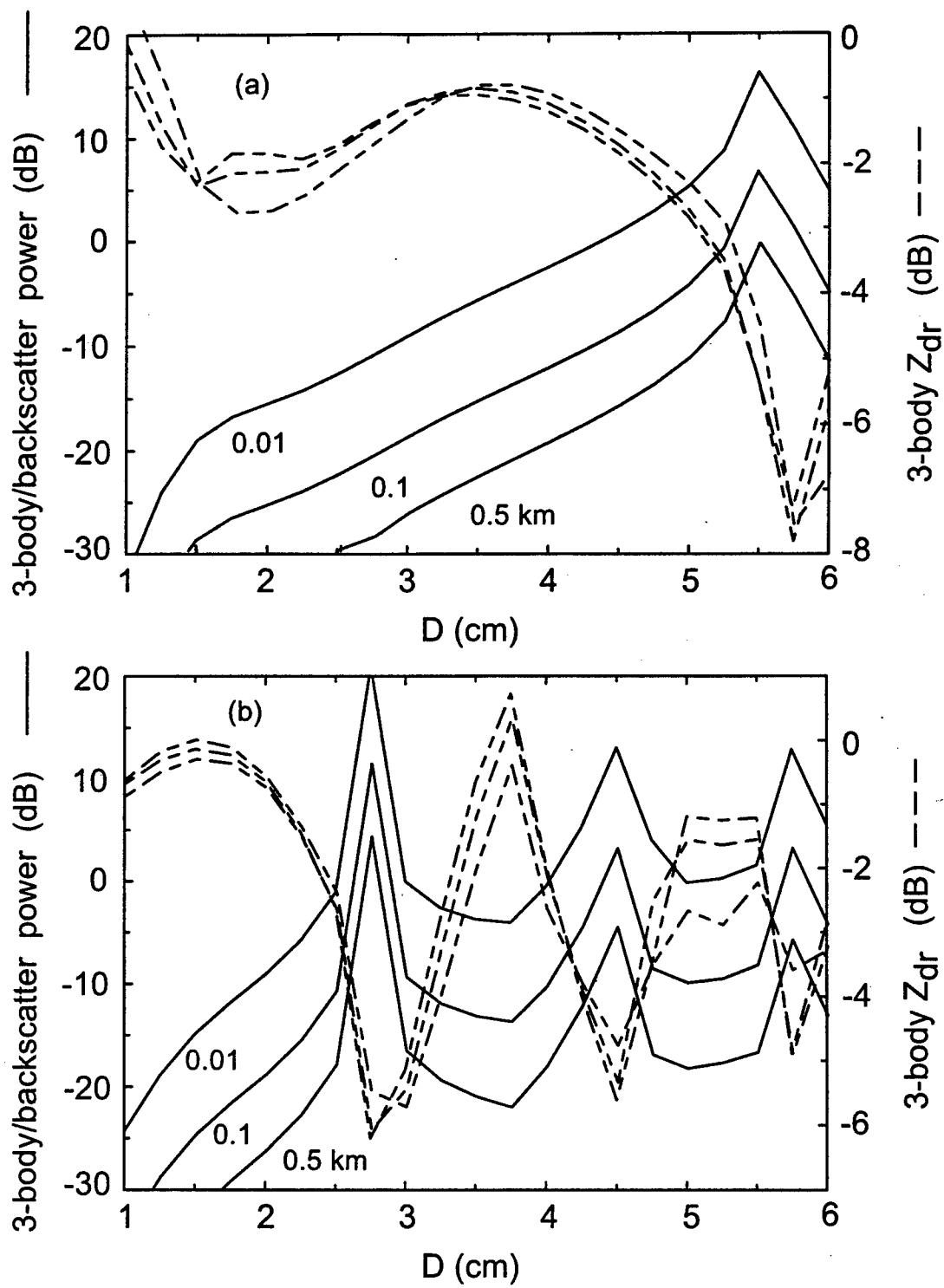


Figure 16: As in Fig. 15 except the statistical ground model is used.

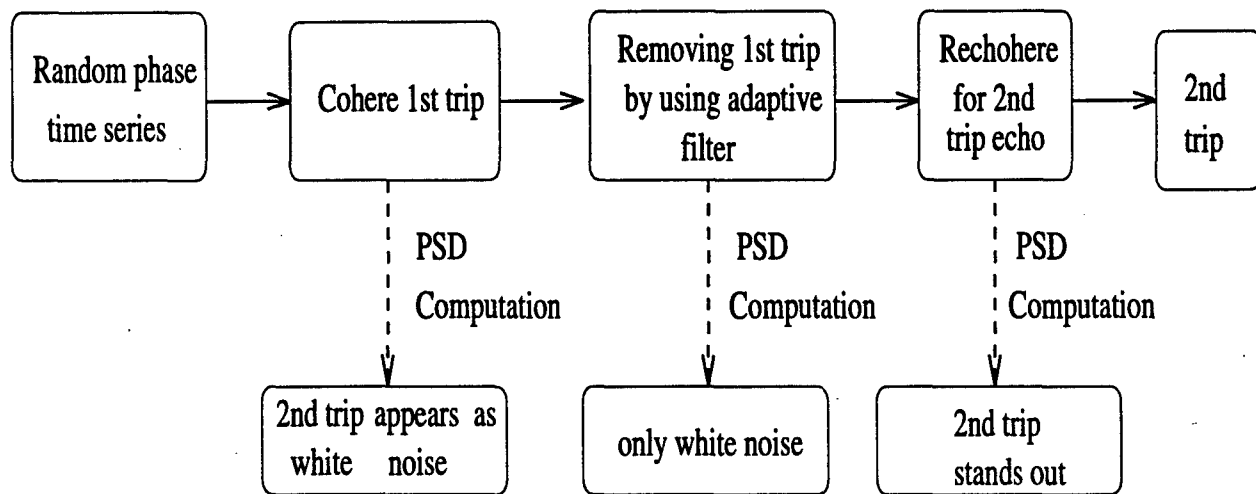


Figure 17: Procedure of random phase processing

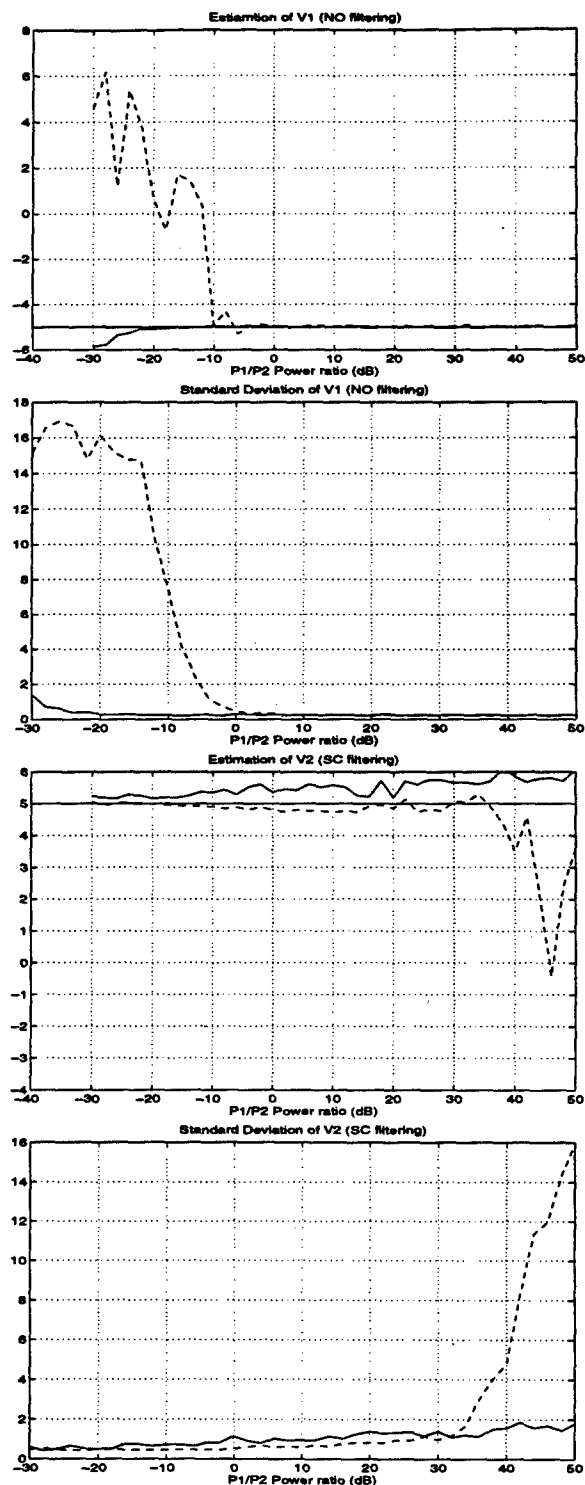


Figure 18: Velocity estimation and its standard deviation for 1st and 2nd trip echos. The dash line stands for the result with phase coding method and the solid line stands for the result with phase/polarization coding.

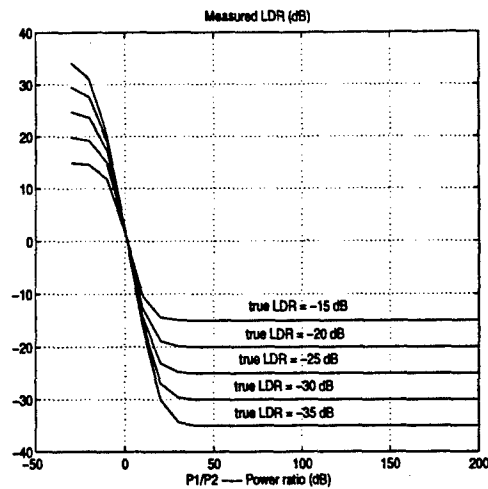


Figure 19: Measured L_{DR} shown as a function of true L_{DR} in the presence of second trip contamination

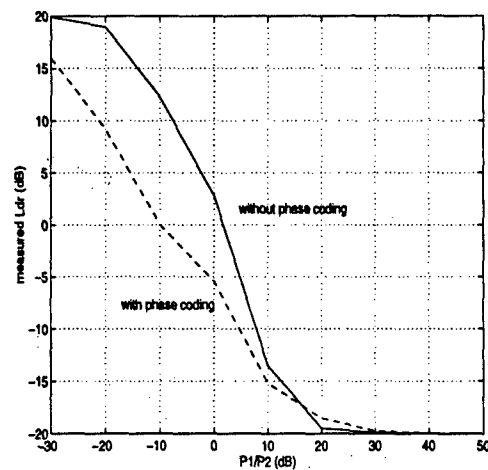


Figure 20: Improvement of measured L_{DR} with phase coding method, the solid line is the measured L_{DR} without phase coding processing, and the dash line is the improved L_{DR} with phase coding method, true L_{DR} is -20dB in this case.